Physics of Fluids

RESEARCH ARTICLE | FEBRUARY 26 2025

Computational fluid dynamics challenge on indoor dispersion of pathogen-laden aerosols

Jordi Pallares ; Alexandre Fabregat ; Akim Lavrinenko ; Nelson Marques ; Bruno Santos ; Gabriele Mosca ; Pedro Obando Vega ; Jure Ravnik ; Nejc Vovk ; Bruño Fraga ; Aleksandra Monka ; Manuel Martínez ; Naomi Mestre-Curto ; Francisco Jose de Souza ; Douglas Fontes ; Natalie Jüngling ; Jennifer Niessner ; Robert Castilla ; Mercè García-Vílchez ; David F. Fletcher ; Kiao Inthavong ; Matjaž Hriberšek ; Paul Steinmann ; Jana Wedel ; Florent Duchaine ; Shriram Sankurantripati ; Leo Amari ; Gábor Janiga ; Cristian Marchioli ; Salvatore Cito

Physics of Fluids 37, 025226 (2025)
https://doi.org/10.1063/5.0252665

Physics of Fluids ARTICLE pubs.aip.org/aip/pof

Computational fluid dynamics challenge on indoor dispersion of pathogen-laden aerosols

Cite as: Phys. Fluids **37**, 025226 (2025); doi: 10.1063/5.0252665
Submitted: 11 December 2024 · Accepted: 30 January 2025 ·
Published Online: 26 February 2025

Jordi Pallares,[1] Alexandre Fabregat,[1,a)] Akim Lavrinenko,[1] Nelson Marques,[2,3] Bruno Santos,[2] Gabriele Mosca,[4] Pedro Obando Vega,[4] Jure Ravnik,[5] Nejc Vovk,[5] Bruño Fraga,[6] Aleksandra Monka,[6] Manuel Martínez,[7] Naomi Mestre-Curto,[7] Francisco Jose de Souza,[8] Douglas Fontes,[9] Natalie Jüngling,[10] Jennifer Niessner,[10] Robert Castilla,[11] Mercè García-Vílchez,[11] David F. Fletcher,[12] Kiao Inthavong,[13] Matjaž Hriberšek,[5] Paul Steinmann,[14] Jana Wedel,[14] Florent Duchaine,[15] Shriram Sankurantripati,[15] Leo Amari,[16] Gábor Janiga,[16] Cristian Marchioli,[17] and Salvatore Cito[1]

AFFILIATIONS

[1]Departament d'Enginyeria Mecànica, Universitat Rovira i Virgili, Av. Països Catalans, 26, 43007-Tarragona, Spain
[2]FS Dynamics Portugal, Rua Fonte dos Corvos 29, Casais da Serra, 2665-305 Milharado, Portugal
[3]Department of Mechanical Engineering, ISEL, Rua Conselheiro Emídio Navarro 35, 1950-062 Lisboa, Portugal
[4]BuildWind, Rue Bara 175, 1070 Brussels, Belgium
[5]Faculty of Mechanical Engineering, University of Maribor, Smetanova 17, SI-2000, Maribor, Slovenia
[6]School of Civil Engineering, University of Birmingham, Edgbaston, Birmingham, B15 2TT, United Kingdom
[7]Eurecat, Centre Tecnològic de Catalunya, Water, Air and Soil Unit, C. Marcel·lí Domingo 2, 43007-Tarragona, Spain
[8]School of Mechanical Engineering, Federal University of Uberlândia, Uberlândia 38400-902, Brazil
[9]Engineering Program, Westmont College, 955 La Paz Rd., Santa Barbara, California 93108, United States of America
[10]Institute for Flow in Additively Manufactured Porous Media, Heilbronn University of Applied Sciences, Max-Planck-Str.. 39, 74081-Heilbronn, Germany
[11]CATMech- Fluid Mechanics Department, Universitat Politècnica de Catalunya, Carrer Colom, 1-11, 08222-Terrassa, Spain
[12]School of Chemical and Biomolecular Engineering, The University of Sydney, Sydney, Australia
[13]Mechanical & Automotive Engineering, School of Engineering, RMIT University, Bundoora, Victoria 3083, Australia
[14]Institute of Applied Mechanics, University of Erlangen Nuremberg, Erlangen, Germany
[15]CERFACS, 42 Avenue Gaspard Coriolis, 31 057 Toulouse, Cedex 01, France
[16]Laboratory of Fluid Dynamics and Technical Flows, Otto von Guericke University of Magdeburg, Germany
[17]Department of Engineering and Architecture, University of Udine, Via delle Scienze 208, 33100 Udine, Italy

[a)]**Author to whom correspondence should be addressed:** alexandre.fabregat@urv.cat

ABSTRACT

This paper presents and discusses the results of the "2024 International Computational Fluid Dynamics Challenge on the long-range indoor dispersion of pathogen-laden aerosols" aimed at assessing the ability of different computational codes and turbulence models to reproduce the dispersion of particles produced by a turbulent natural convection flow enclosed in a room sized cubical cavity. A total of 12 research groups from ten different countries have conducted 15 simulations of the same flow configuration by solving the Reynolds averaged Navier–Stokes (RANS) equations, the unsteady Reynolds averaged Navier–Stokes (URANS) equations or using scale adaptive simulations (SAS), large-eddy simulations (LES), or hybrid (URANS-LES) techniques. Results for the velocity field and the particle dispersion provided by the different simulations are compared extensively, including the reference results provided by a direct numerical simulation (DNS). In general, LES and hybrid methods reproduce the time-averaged flow field correctly, the spatial distribution of the turbulence kinetic energy, and the particle dispersion. The performance of SAS is similar to that of LES and hybrid methods while the predictions of the RANS and URANS simulations exhibit larger deviations with respect to DNS. In general, the particle dispersion is better reproduced by simulations that capture correctly the spatial distribution of the turbulence kinetic energy.

I. INTRODUCTION

Good indoor air quality is important for human health. Long-term exposure to air pollution can cause several health problems (Maroni *et al.*, 1995). The list of potential contaminants is long and includes chemicals, smoke, biological pollutants, and particulate matter (PM), among others (Jones, 1999; Seguel *et al.*, 2017; WHO, 2010). Indoor PM encompasses solid and/or liquid particles suspended in air, and concerns are focused on particles that are 10 micrometers in size or smaller (PM10) because these particles are inhalable and can affect the lungs and the heart (Riley *et al.* 2002; Tan and Zhang, 2003). Indoor PM is generated, among other sources, by cooking, cleaning, and combustion activities, printers, animals, mold, as well as humans, when breathing, speaking, singing, sneezing, or coughing (Li *et al.*, 2017). The pathogen-laden aerosols generated during these respiratory events by an infected person are known to be the route of transmission of some respiratory diseases (Bourouiba, 2021).

Computational fluid dynamics (CFD) has been essential in analyzing and predicting indoor airflows in the last few decades (Li and Nielsen, 2011). Most of the CFD based studies have been oriented toward understanding and improving ventilation strategies (Cuce *et al.* 2019, Yerragolam *et al.*, 2024), determining the exposure to pollutants (Shen *et al.* 2013, Choi *et al.*, 2019; Concilio *et al.*, 2024), analysis of the dispersion and deposition of PM (Xu and Wang, 2017), or establishing the risk of infection by pathogen laden aerosols (Ai and Melikov, 2018, Sheikhnejad *et al.*, 2022; Shim *et al.*, 2023). Simulations of indoor ventilation have been performed mostly using the numerical solutions of the Reynolds averaged Navier–Stokes (RANS) equations and, to a lesser extent, with large-eddy simulations (LES) techniques (Caciolo *et al.* 2012). The relatively high Reynolds number, with length scales on the order of several meters and velocities of several tens of meters per second, makes the current use of direct numerical simulations (DNS) almost unfeasible nowadays due to the extremely high computational cost (Yerragolam *et al.*, 2024; Yang *et al.*, 2022). In addition, the typical forced ventilation strategies encountered in real scenarios, which include free and/or wall jets interacting with thermal stratification and buoyancy effects, produce very different turbulence levels. In turn, this results in different turbulence lengths and time scales, in different locations of the room, which is usually characterized by complex geometry (furniture, persons, etc.) and complex boundary conditions (windows, heaters, fans, etc.). The assessment of the performance of RANS and LES approaches has been analyzed by comparing the numerical predictions with experiments (Bournet and Boulard 2010; Caciolo *et al.* 2012; Villafruela *et al.*, 2013; Gilani *et al.* 2016; van Hooff *et al.*, 2017). This comparison is often influenced by the finite number of measurements that can be obtained experimentally and by the uncertainty of the measurements themselves and of the boundary conditions.

This paper presents and discusses extensive comparisons of numerical simulations of the flow and particle dispersion in a prototypical room. These simulations have been performed by different research groups in the framework of an international CFD challenge. The goal of this collaborative study is to assess the performance of computationally efficient turbulence modeling techniques, specifically those based on LES, SAS, and RANS simulations within a well-defined and controlled flow configuration. We have selected a simplified flow setup that permits the use of DNS, enabling us to obtain comprehensive reference data on turbulent flow and particle dispersion. These data serve as a benchmark for comparison with the LES, SAS, and RANS simulation results. We have considered the enclosed turbulent natural convection flow generated by imposing a temperature difference on two pairs of horizontal and vertical walls of a room-size cubical cavity.

DNS of turbulent natural convection flows in cubical enclosures have been performed for different combinations of heated and cooled walls. In particular, turbulent Rayleigh-Bénard convection (Demou and Grigoriadis, 2019, Vasiliev *et al.*, 2019, Delort-Laval *et al.*, 2022) and the turbulent free convection generated in the side-heated cubical enclosure (Tric *et al.*, 2000; Salat *et al.*, 2004; Kalilainen *et al.*, 2016; Dehbi *et al.*, 2017; Wang *et al.*, 2017) have been extensively investigated. Other combinations of heated and cooled walls include the mixed cavity free convection with simultaneously imposed vertical and horizontal temperature gradients (Hanjalić and Vasić, 1993; Teimurazov *et al.* 2021). In this particular flow configuration, the orientation and the direction of fluid rotation within the large-scale circulation are fixed and determined by the thermally active vertical walls. This is in contrast to the classical Rayleigh–Bénard problem in a cubic cavity, heated from below and cooled from above, with adiabatic vertical walls. In this scenario, the large-scale circulation changes the orientation with a relatively low frequency (Soucasse *et al.*, 2019, Maity *et al.*, 2022), and this introduces a timescale which is much longer than the characteristic time scales associated with the instantaneous turbulent flow structures. Numerical simulations of the laminar and turbulent mixed cavity natural convection have been reported in the range $10^5 \leq Ra \leq 5 \times 10^8$ by Fabregat and Pallares (2020) and at $Ra = 3.6 \times 10^9$ by Lavrinenko *et al.*, (2023), where Ra is the Rayleigh number, the ratio of buoyancy and thermal diffusivity. At such high Ra, the thermal boundary layers on the horizontal walls are fully turbulent, while those attached to the thermally active vertical walls, although unsteady, are essentially laminar. We selected this flow, for which DNS can be obtained, as a prototypical indoor turbulent natural convection flow in a generic room to analyze the turbulent dispersion of particle tracers.

This paper is structured as follows: Sec. II describes the physical model of the mixed cavity configuration, outlines the organization and the challenge framework, and indicates the metrics used for the comparison of the results of the different participants. Section III is devoted to the presentation and discussion of the results. Finally, conclusions and recommendations are outlined in Sec. IV.

II. PROBLEM DEFINITION AND CHALLENGE FRAMEWORK

A. Physical model

We consider the dispersion of particles in a three-dimensional turbulent natural convection flow enclosed in a room-sized cubical cavity. The physical model of the cubical cavity, with dimension $L = 2.5$ m, and the Cartesian coordinates adopted are shown in Fig. 1. The origin of coordinates is located at the center of the cavity. The bottom wall and a vertical wall are kept at a constant and uniform temperature (T_H), larger than the constant and uniform temperature of the top and the vertical opposed wall (T_C). The other two vertical sidewalls are considered perfectly adiabatic. The fluid is air at ambient temperature ($T_0 = (T_H + T_C)/2$) and pressure. The physical properties of the fluid (see Table I) are assumed to be constant with temperature except for the density, which varies linearly with temperature

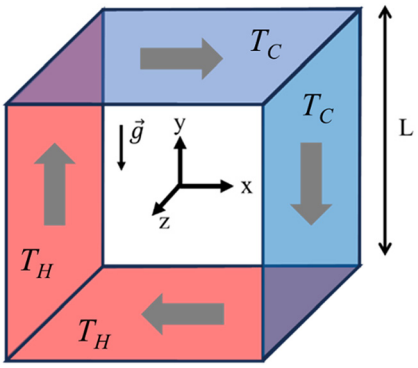

FIG. 1. Sketch of the cubical cavity and the coordinates. Hot/cold walls are indicated in red/blue. The arrows show the rotation of the large-scale flow circulation.

($\rho = \rho_0[1 - \beta(T - T_0)]$). This dependence is only considered in the buoyancy term according to the Boussinesq approximation. Viscous heating and radiation heat transfer are neglected.

The values of the Rayleigh number ($Ra = g\beta(T_H - T_C)L^3/\nu\alpha$) and the Prandtl number ($Pr = \nu/\alpha$) are 3.6×10^9 and 0.7, respectively. In the definitions of these non-dimensional parameters, $\alpha = \frac{k}{\rho_0 C_p}$ is the thermal diffusivity. The flow at lower Rayleigh numbers in this configuration has been analyzed by Fabregat and Pallares (2020), and some quantities at this high Rayleigh number are reported by Lavrinenko *et al.* (2023) and Lavrinenko *et al.* (2024).

We consider the unsteady dispersion of two clouds of solid spherical particles released when the turbulent natural convection flow is statistically fully developed. The initial shape of the clouds is spherical with dimension $D_c = 0.5$ m ($D_c^* = \frac{D_c}{L} = 0.2$), and particle distribution inside the clouds is uniform. Cloud#1 is located near one of the bottom corners of the cavity, where the hot horizontal and vertical walls meet, and the center of cloud#2 is located in the geometrical center of the cavity. The coordinates of the centers of the two clouds with respect to the coordinates shown in Fig. 1 are $x_{c1} = y_{c1} = z_{c1} = -0.4L$ and $x_{c2} = y_{c2} = z_{c2} = 0$, respectively.

The particles are assumed to be perfectly spherical with a constant diameter ($d_p = 0.5\,\mu$m) and with density $\rho_p = 1350\,\text{kg/m}^3$. This relatively small diameter has been selected to minimize the gravitational settling of the particles. Participants were asked to compute the particle dispersion using a Lagrangian method under the one-way coupling hypothesis and according to the following requirements: The equations of particle motion had to be integrated at least during $t^* = t\frac{\alpha\sqrt{Ra}}{L^2} = 150$ non-dimensional time units ($t \approx 700$ s) with a proper time integration step; the number of particles in each cloud had to be larger than 1000. According to the simulations by Lavrinenko *et al.*, (2023), for the flow conditions considered, only a few particles are expected to reach the wall and, by default, for these events, a perfect elastic rebound can be assumed.

B. Challenge framework

The objective of the challenge is to assess the validity of using a computationally affordable turbulence model to reproduce both the flow dynamics and the dispersion of the aerosol cloud in an idealized indoor environment.

The Challenge was officially announced on October 2, 2023. A flyer, included in the supplementary material, was distributed to a mailing list of approximately 400 recipients. This list comprised researchers within the organizers' network, supplemented with emails gathered from journal publications focused on numerical simulations of turbulent natural convection flows and particle dispersion. We received expressions of interest from 30 teams. These teams were provided with the Instructions document, available in the supplementary material. By the submission deadline of May 1, 2024, data had been received from 12 teams, contributing a total of 15 simulations. Each team's results were presented and discussed during an online workshop held on June 20, 2024. Table II provides an affiliation-ordered list of participants, representing academic institutions, research centers and engineering firms.

To prevent misleading collaborations among participants, the challenge was organized as a blind test. Participants were unaware of the other teams until after the data submission deadline, and file exchanges between participants and organizers were conducted via private Google Drive folders for each team. The DNS data published by Fabregat and Pallares (2020) and by Lavrinenko *et al.*, (2023), which were made freely available to the teams during the challenge, were recommended as benchmarks. Participants were required to submit data in ASCII or VTK formats to facilitate post-processing with the open-source multi-platform software ParaView (ParaView, 2024).

Table III summarizes the most important information from the simulations submitted. In addition, the specific details of each turbulence models used and of the models of the different terms of the particle force balance are included as supplementary material. The last column of Table III identifies each specific simulation with a code with two letters. The randomized first letter (from A to L) identifies the team, while the second corresponds to the turbulent modeling used (namely, L for large-eddy simulation, H for hybrid URANS-LES methods, S for scale-adaptive simulation, U for URANS-based simulation, or R for RANS-based simulation). Three teams (F, H, and L) performed the simulations with commercial codes, six teams (B, C, D, G, I, and K) with the open-source OpenFOAM solver, and three teams (A, E, and J) used their own in-house solvers. All the simulations were carried out with finite volume solvers, except for the in-house solvers used by teams A and J, which are based, respectively, on finite element and finite difference techniques for the spatial discretization of the governing equations. The set of fifteen simulations comprises three large-eddy simulations, four hybrid LES-RANS simulations, two scale-adaptive simulations, three URANS-based simulations, and three RANS-based simulations. The teams were instructed to conduct a grid independence test to determine the appropriate mesh resolution. The

TABLE I. Physical properties and parameters of the problem.

Ra	Pr	ρ_0(kg/m^3)	μ (Pa·s)	k(W/m K)	C_p(J/kg K)	β(K^{-1})	L(m)	T_H(°C)	T_C(°C)	T_0(°C)
3.6×10^9	0.7	1.161	1.85×10^{-5}	2.64×10^{-2}	1007	3.33×10^{-3}	2.50	28.11	25.57	26.84

TABLE II. Affiliation of the participating teams. Alphabetical order.

BuildWind SRL	Belgium
CERFACS	France
Eurecat	Spain
Federal University of Uberlândia - Westmont College	Brazil - USA
FS Dynamics Portugal	Portugal
Heilbronn University of Applied Sciences	Germany
Otto von Guericke University of Magdeburg	Germany
RMIT University - The University of Sydney	Australia
Universitat Politècnica de Catalunya	Spain
University of Birmingham	UK
University of Erlangen Nuremberg - University of Maribor	Germany - Slovenia
University of Maribor	Slovenia

selected grids, along with the minimum and maximum grid spacings, are reported in Table III. The value of y^+ corresponding to the minimum distance of the nodes to the horizontal walls, where the boundary layers are turbulent, is 0.3 for the DNS grid ($\Delta x_{min}=1.6\times10^{-4}$ L). For reference, $\Delta x_{min}=5\times10^{-4}$ L corresponds to $y^+=0.9$ and $\Delta x_{min}=10^{-3}$ L to $y^+=1.8$. All teams employed hexahedral elements for their meshes, except for team A, which adopted a grid composed of tetrahedra with two layers of prisms attached to the walls. The LES of team L used a grid of 7×10^6 nodes, while the other two LES teams employed finer grids, with team A using 91×10^6 nodes and team J using 64×10^6 nodes. The number of elements of the meshes for the hybrid simulations are about one order of magnitude smaller and ranges between 2 and 8×10^6 nodes. SAS were performed with grids between 3 and 4×10^6 nodes. The grids selected for URANS and RANS-based simulations generally contain a moderate number of elements, ranging from 0.03 to 4.8×10^6 nodes, except for the simulation of team F, which used 21.2×10^6 nodes. Non-uniform grids stretched toward the walls were used by all teams, except team J, which used a uniform grid. The minimum non-dimensional grid spacings, scaled with the size of the cavity, located near the walls are of order 10^{-4}–10^{-3} and most of the non-dimensional maximum grid spacings, located near the center of the cavity are of order 10^{-2}, with the exception of teams J and H, which used minimum grid sizes of order 10^{-3}. These minimum grid spacings compare reasonably well with the DNS estimations of the time and wall-averaged temperature boundary layer thickness ($\delta/L=(2Nu)^{-1}$, see for example Scheel and Schumacher, 2014) for the vertical ($Nu_v=78$, $\delta_v/L=6.4\times10^{-3}$) and horizontal walls ($Nu_h=112$, $\delta_h/L=4.4\times10^{-3}$). Also good is the estimation of the Kolmogorov length scale ($\eta/L\approx10^{-3}$) for a Rayleigh-Bénard flow at $Ra=3.6\times10^9$ and $Pr=0.7$ (Scheel *et al.*, 2013). The temporal discretization of the governing flow equations for the LES, performed with the finer grids, is explicit (third order for team A and second order for team J), while for the hybrid, SAS and URANS simulations the discretization is implicit. The time steps employed by the different teams range from 3.5×10^{-5} s, for the finest grid, to 2×10^{-1} s for the coarser grids. The minimum number of particles per cloud was set by the organizers according to preliminary numerical tests that showed that the particle dispersion rate metrics, which are presented and described below, in Subsec. II C, were essentially independent for clouds with 1000 or more particles. The gravity and drag forces were considered by all the teams in the particle force balance. In any case, the terminal velocity of the particles is 10 μm/s and consequently gravity is not expected to play a significant role in the dispersion which is monitored during 700 s. The lift force and thermophoresis, included in the particle force balance by some teams, are also expected to have a very limited effect, because of the relatively small density ratio between the fluid and the particles and the reduced values of the temperature gradients where the particle dispersion takes place (i.e., outside the thin thermal boundary layers near the thermally active walls). Random walk models are incorporated in the motion of the particles to account for the effect of turbulence fluctuations in simulations using SAS, URANS or RANS.

C. Metrics for the comparison of the results

Participants were asked to submit the surface averaged Nusselt numbers on the vertical (Nu_v) and horizontal (Nu_h) walls. These are defined as $Nu_v=\langle q_v''\rangle L/k(T_H-T_C)$ and $Nu_h=\langle q_h''\rangle L/k(T_H-T_C)$, where $\langle q_v''\rangle$ and $\langle q_h''\rangle$ are the surface averaged wall heat fluxes on the vertical and horizontal walls, respectively.

The deviations, with respect to DNS, of the predictions of the velocity, temperature, and turbulence kinetic energy profiles along the wall bisectors of the vertical symmetry plane of the cavity ($z=0$), were evaluated by computing the root mean squared differences. First, we interpolated the data submitted by the different teams onto the DNS mesh and computed the root mean squared values as

$$\sigma_\phi=\sqrt{\frac{\sum_{i=1}^{i=N^{DNS}}\left(\phi_i^X-\phi_i^{DNS}\right)^2}{N^{DNS}}}, \tag{1}$$

where σ_ϕ is the rms for the quantity ϕ, which can correspond to velocity, temperature or turbulence kinetic energy, ϕ_i^X is the data of team X interpolated onto the DNS mesh, ϕ_i^{DNS} is the data corresponding to the DNS profiles and N^{DNS} is the number of grid points along the wall bisectors used in the DNS.

The square of the average distance, or separation, of all possible particle pairs has been used to monitor the dispersion of the two particle clouds. We defined three quantities, given in Eqs. (2)–(4) to measure, respectively, the three-dimensional dispersion within the cavity (D_{xyz}^{*2}), the dispersion in the plane of rotation of the large-scale circulation (D_{xy}^{*2}) and the dispersion along the z-direction (D_z^{*2}), that corresponds to the direction of the main alignment of the rotation vector of the large-scale flow (see Fig. 1).

$$D_{xyz}^{*2}=\frac{1}{N}\sum_{i,j}\left(\left[x_i^*-x_j^*\right]^2+\left[y_i^*-y_j^*\right]^2+\left[z_i^*-z_j^*\right]^2\right), \tag{2}$$

$$D_{xy}^{*2}=\frac{1}{N}\sum_{i,j}\left(\left[x_i^*-x_j^*\right]^2+\left[y_i^*-y_j^*\right]^2\right), \tag{3}$$

$$D_z^{*2}=\frac{1}{N}\sum_{i,j}\left(\left[z_i^*-z_j^*\right]^2\right). \tag{4}$$

In Eqs. (2) to (4), N is the total number of possible particle pairs, which is related to the total number of particles in each cloud, n, as

TABLE III. Summary of the simulations details.

Team	Code	Turbulence	Spatial discretization	Grid	$\Delta x_{min}/\Delta x_{max}$	Temporal discretization[a]	#particles/cloud	Particle forces	Code
A	AVBP (Schønfeld and Rudgyard, 1999; Duchaine *et al.*, 2021)	LES: WALE	Finite element. 3rd order	91M tetrahedral/prism	2.5×10^{-3} 2.0×10^{-2}	Explicit. 3rd order $\Delta t_f = \Delta t_p = 3.5 \times 10^{-5}$ s	2000	Drag Gravity	A-L
B	OpenFOAM 2106 (Weller *et al.*, 1998)	URANS: k-ε	Finite volume. 1st order upwind	0.4M hexahedral (75 × 75 × 75)	6.0×10^{-3} 2.5×10^{-2}	Implicit. 1st order $\Delta t_f = \Delta t_p = 10^{-1}$ s	1440	Drag Gravity Random-Walk	B-U
C	OpenFOAM 11 (Weller *et al.*, 1998)	SAS: k-ω SST	Finite volume. 2nd order	3.2M hexahedral (147 × 147 × 147)	4.7×10^{-4} 1.3×10^{-2}	Implicit. 1st order $\Delta t_f = 2 \times 10^{-2}$ s $\Delta t_p = 5 \times 10^{-3}$ s	1021	Drag Gravity Random-Walk	C-S
D	OpenFOAM 2112 (Weller *et al.*, 1998)	RANS: k-ω	Finite volume. 2nd order	4.8M hexahedral (168 × 168 × 168)	2.4×10^{-3} 2.0×10^{-2}	$\Delta t_p = 5 \times 10^{-3}$ s	1000	Drag Lift Gravity Random-Walk	D-R
E	UNSCYFL3D (Velasco *et al.*, 2022)	DES: SST URANS: SST	Finite volume. 2nd order	2.0M hexahedral (125 × 125 × 125)	8.0×10^{-4} 5.6×10^{-2}	Implicit. 2nd order $\Delta t_f = \Delta t_p = 10^{-1}$ s	55 000	Drag Gravity Thermo-phoresis Random-Walk	E-H E-U
F	STAR-CCM+ 2022.1.1 (STAR-CCM+, 2024)	RANS: k-ω SST	Finite volume. 1st order	21.2M hexahedral (276 × 276 × 276)	2.0×10^{-3} 1.2×10^{-2}	$\Delta t_p = 4 \times 10^{-2}$ s	1500	Drag Gravity	F-R
G	OpenFOAM 11 (Weller *et al.*, 1998)	DES: k-ω SST	Finite volume. 2nd order	4.2M hexahedral (161 × 161 × 161)	5.1×10^{-4} 1.3×10^{-2}	Implicit. 1st order $\Delta t_f = \Delta t_p = 10^{-2}$ s	10 000	Drag gravity random-walk	G-H
H	Ansys Fluent, 2024R1 (Ansys Fluent, 2024)	SAS: k-ω SST SBES using LES: WALE, RANS: k-ω SST	Finite volume. 2nd order	8.0M unstructured hexahedral	4.0×10^{-4} 6.4×10^{-3}	Implicit. 2nd order $\Delta t_p = 10^{-2}$ s	1000	Drag gravity	G-S H-H
I	OpenFOAM 11 (Weller *et al.*, 1998)	DES: k-ω SST	Finite volume. 2nd order	1.0M hexahedral (100 × 100 × 100)	2.8×10^{-4} 1.7×10^{-2}	Implicit. 1st order (max. Δt = 0.017 s)	2500	Drag gravity random-walk	I-H
J	MultiFlow3D (Fraga *et al.*, 2016; Monka *et al.*, 2023)	LES: Smagorinsky	Finite difference 2nd order	64M hexahedral (400 × 400 × 400)	2.5×10^{-3} 2.5×10^{-3}	Explicit. 2nd order $\Delta t_f = \Delta t_p = 5 \times 10^{-3}$ s	1500	Drag gravity lift Added mass	J-L
K	OpenFOAM 8 (Weller *et al.*, 1998)	RANS: k-ε	Finite volume. 2nd order	0.03M (prisms + unstructured hexahedra)	5.5×10^{-3} 4.0×10^{-2}	$\Delta t_p = 10^{-1}$ s	1464	Drag gravity lift	K-R
L	STAR-CCM+ 2021.3 (STAR-CCM+, 2024)	LES: WALE URANS: k-ε	Finite volume. 2nd order	7M hexahedral (191 × 191 × 191) 2M hexahedral (126 × 126 × 126)	8.0×10^{-4} 7.2×10^{-3} 8.0×10^{-4} 1.8×10^{-2}	Implicit. 2nd order $\Delta t_f = 1.6 \times 10^{-2}$ s Implicit. 2nd order $\Delta t_f = 10^{-1}$ s	5016	Drag gravity pressure gradient	L-L L-U

[a]Δt_f: Time step for the flow equations. Δt_p: Time step for the particle equations.

$$N = \sum_{k=1}^{n-1} (n-k) = \frac{n(n-1)}{2}. \tag{5}$$

According to the definitions of Eqs. (2) to (4)

$$D^{*2}_{xyz} = D^{*2}_{xy} + D^{*2}_{z}. \tag{6}$$

The limiting dimensional values of the mean squared distance, D^2_{xyz}, corresponding to a perfectly uniform distribution of particles in a cubical box, with dimension L, can be computed as

$$\begin{aligned} &D^2_{xyz}(t\to\infty) \\ &= \frac{1}{L^6}\int_{z_2=-L/2}^{z_2=L/2}\int_{y_2=-L/2}^{y_2=L/2}\int_{x_2=-L/2}^{x_2=L/2} \\ &\times\left\{\int_{x_1=-L/2}^{x_1=L/2}\int_{y_1=-L/2}^{y_1=L/2}\int_{x_1=-L/2}^{x_1=L/2}\right. \\ &\left.\times\left[\left\langle (x_1-x_2)^2+(y_1-y_2)^2+(z_1-z_2)^2\right\rangle dx_1\,dy_1\,dz_1\right]\right\} \\ &dx_2\,dy_2\,dz_2 = \frac{L^2}{2}. \end{aligned} \tag{7}$$

Similarly, $D^2_{xy}(t\to\infty) = \frac{L^2}{3}$ and $D^2_{z}(t\to\infty) = \frac{L^2}{6}$.

Initially, the particles are released in spherical clouds, with diameter D_c, and particle distribution is uniform. The corresponding dimensional value of D^2_{xyz} can be computed as

$$\begin{aligned} &D^2_{xyz}(t=0) \\ &= \frac{1}{\left(\frac{\pi D_c^3}{6}\right)^2}\int_{\varphi_2=0}^{\varphi_2=2\pi}\int_{\theta_2=0}^{\theta_2=\pi}\int_{r_2=0}^{r_2=D_c/2} \\ &\times\left\{\int_{\varphi_1=0}^{\varphi_1=2\pi}\int_{\theta_1=0}^{\theta_1=\pi}\int_{r_1=0}^{r_1=D_c/2}\left[\left\langle (r_1\sin\theta_1\cos\varphi_1 - r_2\sin\theta_2\cos\varphi_2)^2\right.\right.\right. \\ &+(r_1\sin\theta_1\sin\varphi_1 - r_2\sin\theta_2\sin\varphi_2)^2 \\ &+(r_1\sin\theta_1\sin\varphi_1 - r_2\sin\theta_2\sin\varphi_2)^2 \\ &\left.\left.\left.+(r_1\cos\theta_1 - r_2\cos\theta_2)^2\right\rangle r_1^2\sin\theta_1 dr_1\,d\theta_1\,d\varphi_1\right]\right\} \\ &\times r_2^2\sin\theta_2 dr_2\,d\theta_2\,d\varphi_2 = \frac{3D_c^2}{10}. \end{aligned} \tag{8}$$

Similarly, $D^2_{xy}(t=0) = \frac{D_c^2}{5}$ and $D^2_{z}(t=0) = \frac{D_c^2}{10}$.

These limiting dimensional values can be used to bound the non-dimensional values of the mean squared average distances between 0 and 1

$$D^{**2}_{xyz} = \frac{D^2_{xyz} - D^2_{xyz}(t=0)}{D^2_{xyz}(t\to\infty) - D^2_{xyz}(t=0)}, \tag{9}$$

$$D^{**2}_{xy} = \frac{D^2_{xy} - D^2_{xy}(t=0)}{D^2_{xy}(t\to\infty) - D^2_{xy}(t=0)}, \tag{10}$$

$$D^{**2}_{z} = \frac{D^2_{z} - D^2_{z}(t=0)}{D^2_{z}(t\to\infty) - D^2_{z}(t=0)}. \tag{11}$$

In this case, the following inequality holds for the non-dimensional distances, $D^{**2}_{xyz} \neq D^{**2}_{xy} + D^{**2}_{z}$.

III. RESULTS AND DISCUSSION

A. Flow and heat transfer

Figure 2 shows the differences, expressed as a percentage, of the predictions of the surface averaged Nusselt numbers on the horizontal and vertical walls with respect to the DNS results ($Nu_h^{DNS} = 112$, $Nu_v^{DNS} = 78$). In general, the predictions obtained with the URANS or RANS approaches show larger deviations (±25%) than the LES/hybrid or SAS methods (−12%). The two SAS simulations, carried out with similar grid resolutions, exhibit differences smaller than 5%. Four of the simulations performed with the LES/hybrid techniques (A-L, L-L, G-H, and H-H) also show deviations smaller than 5%. These simulations used, respectively, grids of 91, 7, 4.2, and 8 M nodes, while the simulations E-H and I-H, with differences larger than 5% were carried out with coarser meshes of 2 and 1 M nodes. The LES of team J also show differences larger than 5%, despite the use of a uniform grid with 64 M nodes.

The time averaged profiles of the non-dimensional velocity, temperature, and turbulence kinetic energy along the horizontal and vertical bisectors of the vertical symmetry plane of the cavity are plotted in Figs. 3–5, respectively. The length, time, and temperature scales, used to obtain the non-dimensional variables, are the size of the cavity, L, the convection time, $L^2/\alpha\sqrt{Ra}$, and the temperature increment, $T_H - T_C$ (i.e., $x_i^* = x_i/L$, $u_i^* = u_i L^2/\alpha\sqrt{Ra}$ and $\theta = (T - T_o)/(T_H - T_C)$). The DNS predictions are indicated using symbols and the results of the various teams using lines of different colors. The profiles of the teams that presented two simulations (E, G and L) are plotted with the same color but with a different line pattern. For clarity, we plotted LES/hybrid and SAS/URANS/RANS results separately. Figures 3 and 4, corresponding to the velocity and temperature profiles, respectively, show that, overall, the predictions of the LES/hybrid simulations exhibit less variability and a better agreement with the DNS. An exception is the simulation I-H, performed with a relatively coarse mesh. This simulation shows significant deviations with respect to the

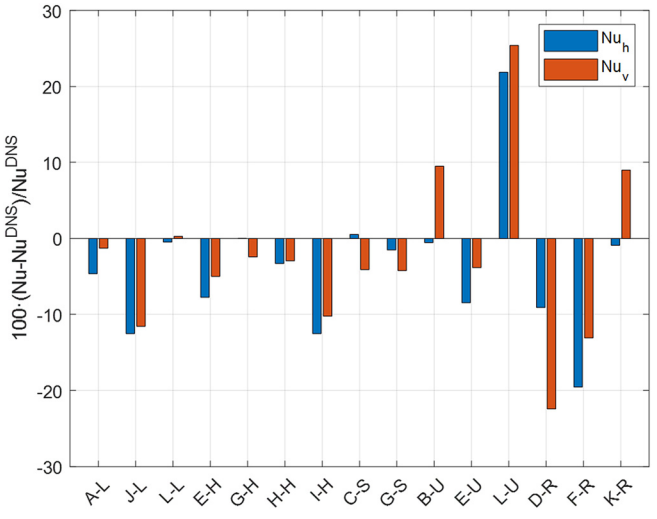

FIG. 2. Differences in the surface-averaged Nusselt numbers on the horizontal (Nu_h) and vertical (Nu_v) walls.

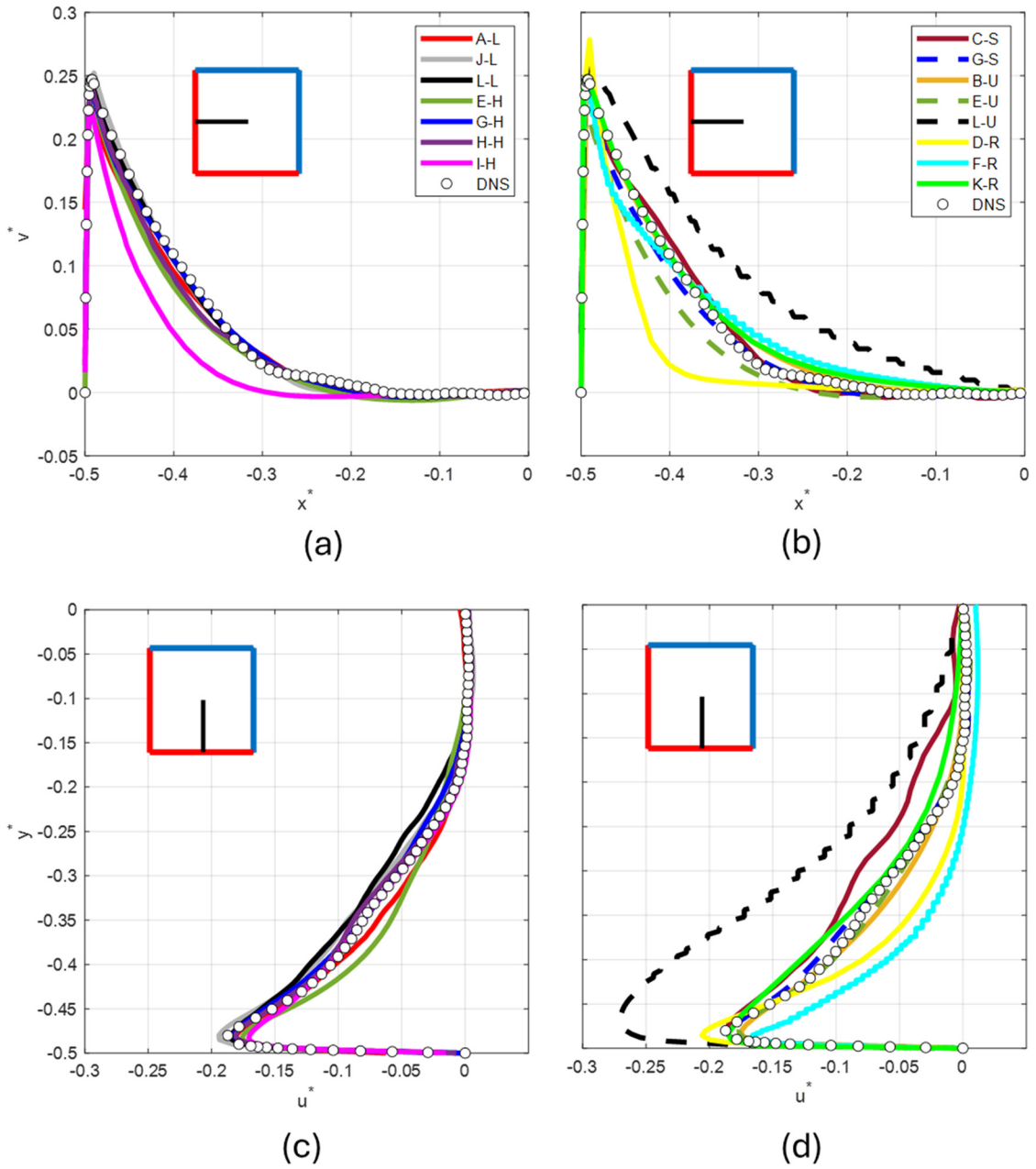

FIG. 3. Non-dimensional time-averaged velocity profiles along the horizontal (a) and (b) and vertical (c) and (d) bisectors of the vertical symmetry plane of the cavity ($z = 0$).

DNS in the horizontal velocity profile of Fig. 3(a) and in the temperature profiles of Figs. 4(a) and 4(c).

The turbulence kinetic energy profiles, plotted in Fig. 5, also reveal the better overall performance of LES/hybrid techniques. The RANS simulations [Figs. 5(b) and 5(d)] tend to underpredict the intensity of the fluctuations near the wall and to overpredict them near the center of the cavity. This is also observed for the URANS simulation B-U, which was carried out with a relatively coarse mesh (0.4 M nodes) and a first-order spatial discretization. The SAS results (C-S and G-S) and the URANS, E-U, show predictions that are closer to the DNS. We quantified the departure, from the DNS, of the profiles shown in Figs. 3–5, by computing the root mean squared differences, defined in Eq. (1). The values are plotted in Fig. 6(a), for the velocity and temperature profiles, and in Fig. 6(b) for the turbulence kinetic energy. These figures summarize the differences already highlighted, when discussing the profiles of the time-averaged velocity, temperature and turbulence kinetic energy. Figure 6(b) indicates that LES/Hybrid techniques, along with SAS, provide a relatively accurate prediction of the turbulence

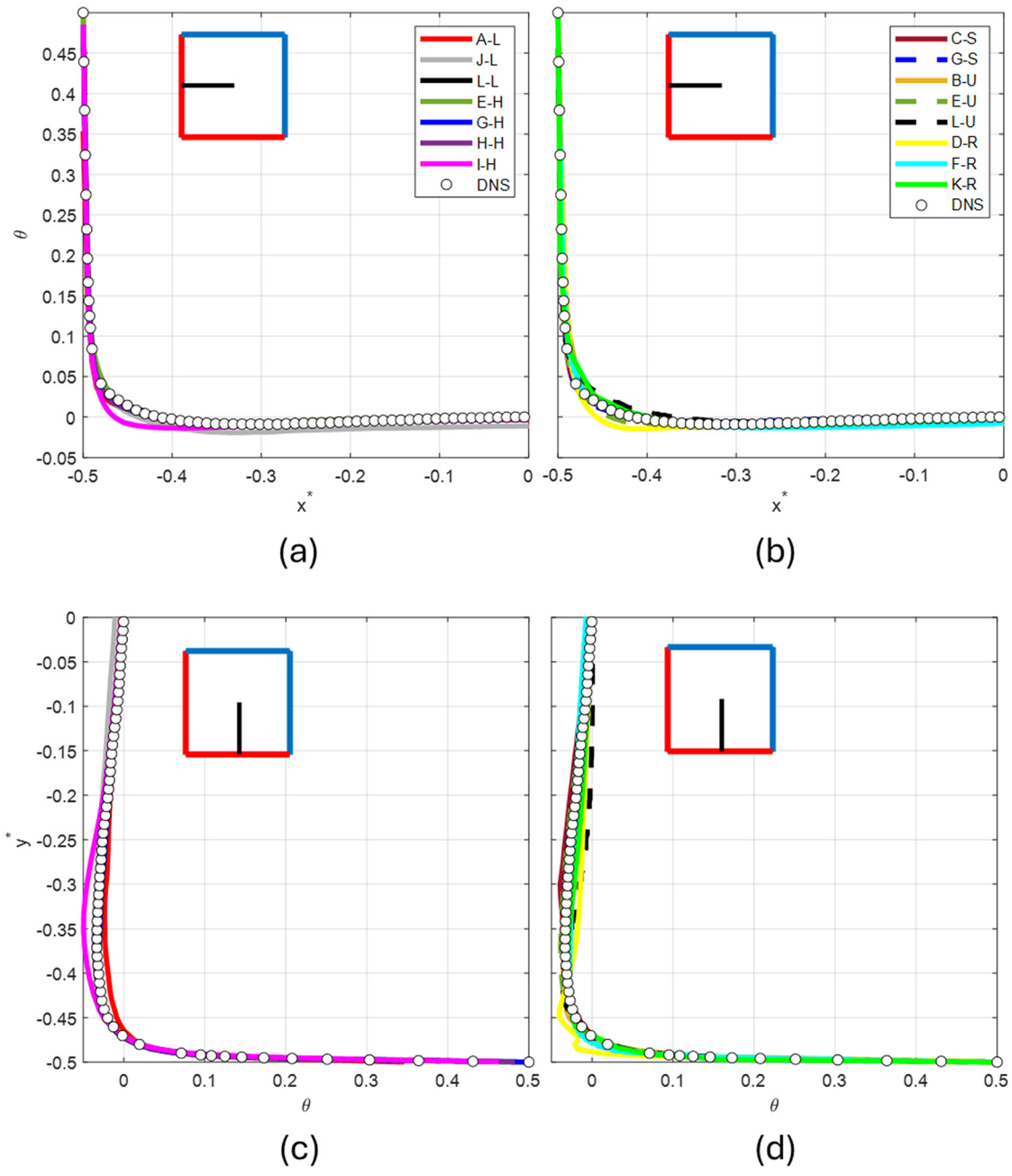

FIG. 4. Non-dimensional time-averaged temperature profiles along the horizontal (a) and (b) and vertical (c) and (d) bisectors of the vertical symmetry plane of the cavity ($z = 0$).

kinetic energy, especially when compared with the RANS and URANS methods. Exceptions are the simulation I-H, that, as indicated above, exhibits relatively large deviations of the velocity profiles and the URANS simulation E-U, which reproduces well the turbulence kinetic energy [Figs. 5(b) and 5(d)] and shows moderate differences with respect to DNS in the velocity and temperature profiles [Figs. 6(a)].

The spatial distribution of turbulence kinetic energy within the cavity plays a crucial role in the three-dimensional dispersion of particle clouds. To illustrate this, the two-dimensional distributions of the turbulence kinetic energy in the vertical symmetry plane of the cavity ($z = 0$) and in the horizontal mid plane ($y = 0$) are plotted in Figs. 7–10. The initial positions of the particle clouds are indicated by the white circles in Figs. 7(a), 8(a), 9(a) and 10(a), corresponding to the

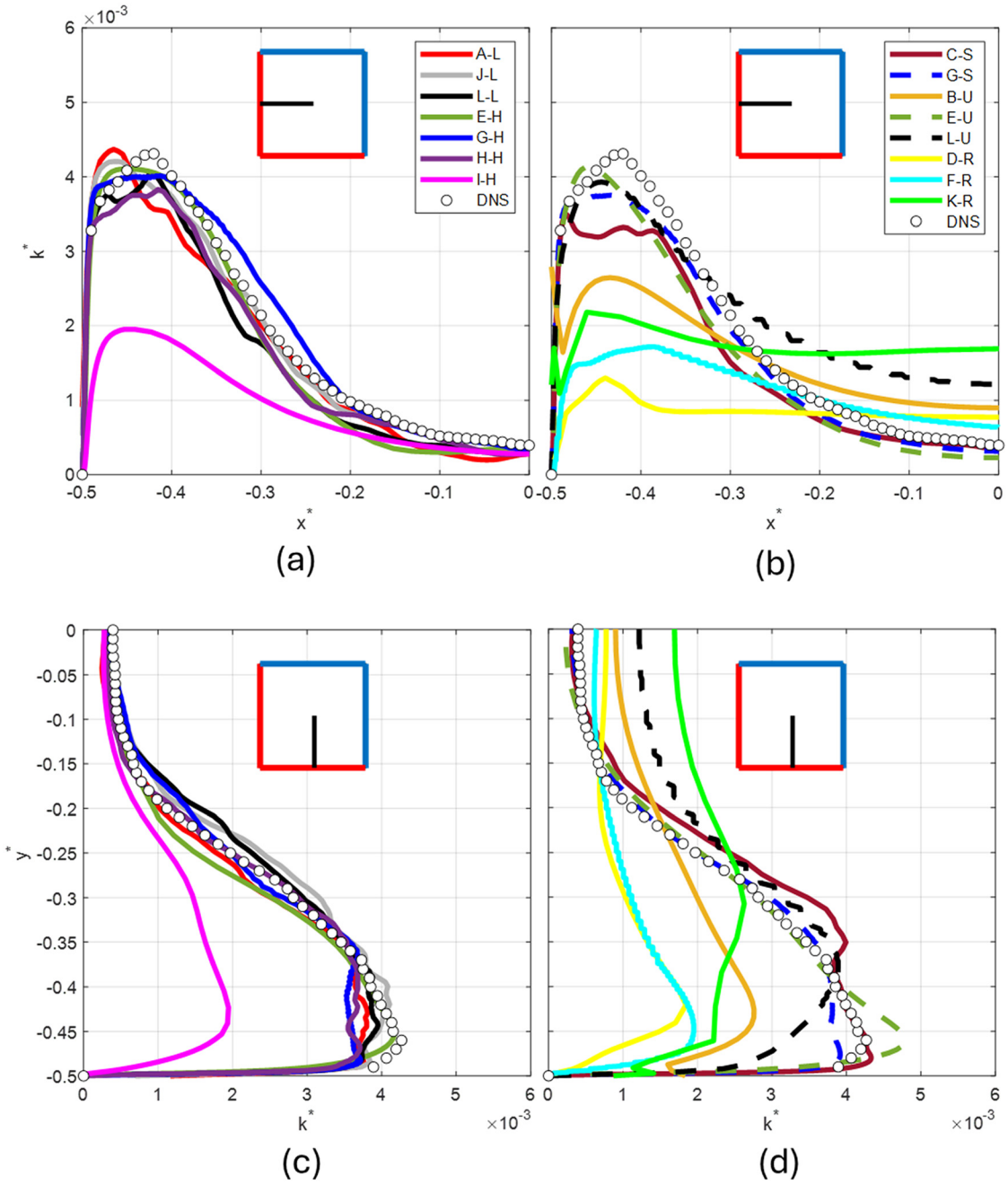

FIG. 5. Non-dimensional turbulence kinetic energy profiles along the horizontal (a) and (b) and vertical (c) and (d) bisectors of the vertical symmetry plane of the cavity ($z = 0$).

DNS results. Cloud#1 is shown with a dashed line and Cloud#2, with a continuous line. A local minimum in fluctuation intensities can be observed near the center of the cavity. This area is an almost stagnant region in terms of time-averaged behavior, as indicated by the velocity profiles shown in Fig. 3. This is precisely where Cloud#2 originates. The turbulence kinetic energy reaches a local maximum along the path of large-scale flow recirculation, occurring where the time-averaged velocity declines from its peak (located very close to the wall) to a local minimum at the center of the cavity [see Figs. 3(a) and 5(a)]. The turbulence kinetic energy exhibits localized maxima near the top left and bottom right corners of the vertical symmetry plane of the cavity, where the hot and cold walls meet [see, for example, Fig. 7(a)]. The

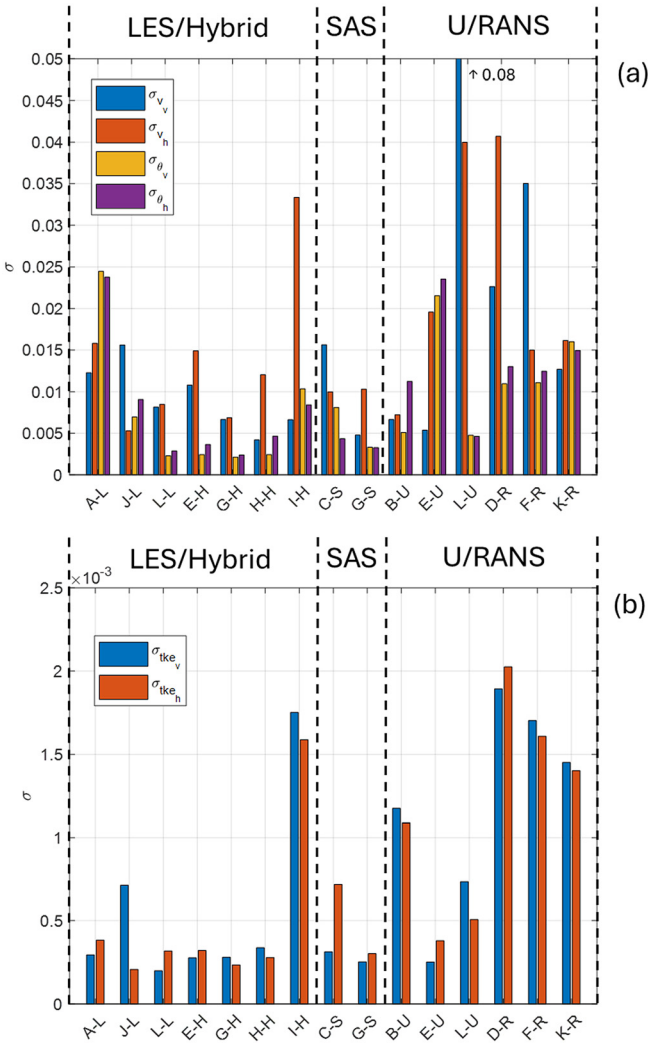

FIG. 6. Root mean squared differences, between the different predictions and the DNS, in the profiles of (a) velocity and temperature and (b) turbulence kinetic energy along the horizonal and vertical bisectors of the vertical symmetry plane of the cavity ($z = 0$). The values of the bars above the maximum scale of the vertical axis are indicated.

distribution of the turbulence kinetic energy is essentially uniform along the z direction of the cavity, as shown in Fig. 8(a). This direction is indeed aligned to the rotation axis of the large-scale flow recirculation. As shown in Fig. 8(a), the effect of the adiabatic walls, located at $z = -1/2$ and $z = 1/2$, in the distribution of the turbulence kinetic energy is restricted to areas that are very close to these walls.

Figures 7 and 8 show that, globally, the LES/hybrid techniques provide predictions of the turbulence kinetic energy spatial distributions in the $z = 0$ (Fig. 7) and $y = 0$ (Fig. 8) planes that closely match the DNS benchmark case. However, simulation I-H underpredicts, in general, the level of the fluctuations along the path of the large-scale flow recirculation [see Figs. 7(h) and 8(h)]. The predictions of the SAS, shown in Figs. 9(b), 9(c), 10(b), and 10(c) agree well with the DNS. The contours of the turbulence kinetic energy of the three URANS are plotted in Figs. 9(d)–9(f) and 10(d)–10(f). The simulation E-U [Figs. 9(e) and 10(e)], carried out using the k-ω SST model and a grid of 2 M cells, agrees with the DNS while the simulation L-U [Figs. 9(f) and 10(f)], albeit sharing the same grid resolution, exhibits larger differences with respect to the DNS using the k-ε model. The simulations B-U [Figs. 9(d) and 10(d)], also carried out with a k-ε model but on a relatively coarse grid (0.4 M cells) shows larger deviations in the distributions of the turbulence kinetic energy with respect to the DNS. The three RANS-based simulations (D-R, F-R, and K-R) generally underpredict the levels of the turbulence kinetic energy, as shown in Figs. 9(g)–9(i) and 10(g)–10(i) irrespective of the turbulence model (k-ε or k-ω) or grid resolution used (see Table III). Overall, the evaluation of the local turbulence kinetic energy distribution is characterized by significantly higher uncertainty in comparison with the velocity and temperature mean profiles.

In summary, the comparative study performed indicates that, in general, SAS methods predict the heat transfer rates and the time-averaged distributions of velocity, temperature, and turbulent kinetic energy as accurately as LES or hybrid techniques, provided the mesh resolutions are comparable.

B. Particle dispersion

Under statistically fully developed flow conditions, we have considered the independent dispersion of two initially spherical particle clouds of identical size. Cloud#1 is released near one corner of the cavity and Cloud#2, in the center of the cavity (see Fig. 11, Multimedia available online). It can be seen that Cloud#1 is rapidly advected by the large-scale recirculation while particles belonging to Cloud#2 are progressively dispersed within the nearly stagnant center of the cavity and eventually are transported by the large-scale recirculation near the vertical or horizontal thermally active walls.

The time evolutions, predicted by the DNS, of the non-dimensional mean squared values of the particle separations; D^{**2}_{xyz}, D^{**2}_{xy} and D^{**2}_{z}, defined in Eqs. (9)–(11), are plotted in Fig. 12. Figure 12(a) corresponds to Cloud#1 and Fig. 12(b), to Cloud#2. To evaluate the variability of the turbulent dispersion of the two particle clouds, we have computed the ensemble average of 40 time-evolutions (20 for each cloud) of the squared particle separations for clouds released at different times during a period of 40 non-dimensional time units. The vertical span of the shaded areas in Fig. 12 corresponds to plus/minus one standard deviation of the instantaneous mean values, which are plotted with continuous lines. The red, green and blue lines indicate the evolution of D^{**2}_{xyz}, D^{**2}_{xy} and D^{**2}_{z}, respectively. In Fig. 12(a), corresponding to Cloud#1, the shaded areas for the different particle separations have been indicated with the same color code (i.e., light red for D^{**2}_{xyz}, light green for D^{**2}_{xy} and light blue for D^{**2}_{z}). On the other hand, for Cloud#2, the time evolutions of D^{**2}_{xyz}, D^{**2}_{xy} and D^{**2}_{z} as well as their standard deviations are very similar and, for clarity, in Fig. 12(b), the gray shaded area corresponds to the standard deviation of D^{**2}_{z}, which is the largest one.

It can be seen that the time-evolutions of the three mean squared separations of the cloud released in the center of the cavity [Fig. 12(b)] follow, on average, the same trend and reach their limiting values, corresponding to the perfectly mixed situation ($D^{**2}_{xyz} = D^{**2}_{xy} = D^{**2}_{z} = 1$), at about 80 non-dimensional time units. Considering an average non-dimensional velocity scale of 0.1 for the large-scale circulation

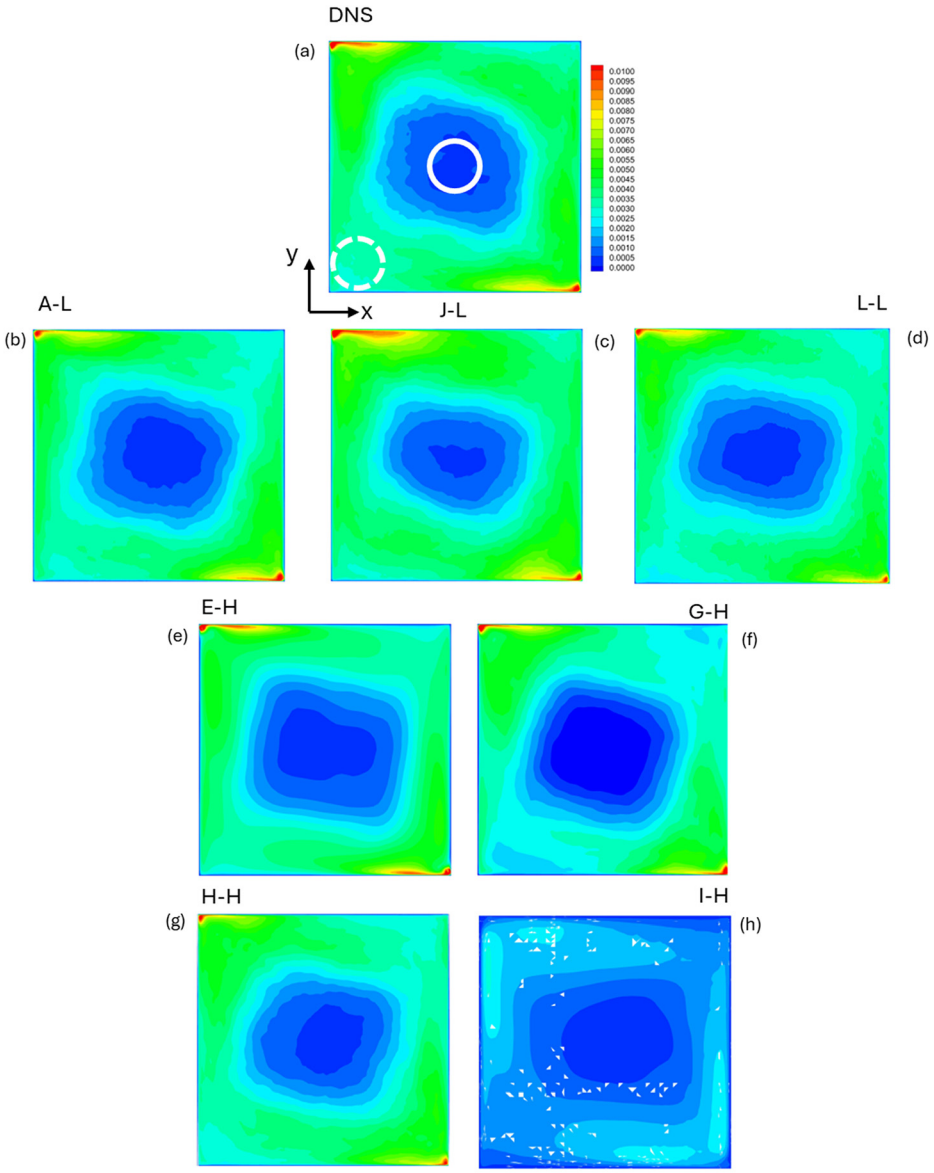

FIG. 7. Contours of the turbulence kinetic energy on the vertical symmetry plane of the cavity ($z = 0$).

(see. Figure 3). Such a span corresponds to approximately two large-eddy turnover times. In contrast, the time evolutions of the separations of the particles released near one corner of the cavity [Cloud#1, Fig. 12(a)] behave distinctly. While the mean separation within the plane of the large-scale circulation, D_{xy}^{**2}, reaches the value of a perfectly uniform particle distribution, relatively fast (at about 40 non-dimensional time units), the mean separation of the particles along the z direction increases, for $t^* > 10$, at a lower rate and reaches the limiting value only at $t^* \approx 100$. This indicates a more effective mixing within the plane of the large-scale circulation than along the z direction. Note also that the release of Cloud#2 in the geometric center of the cavity is more effective for dispersing particles along the z direction than the release of Cloud#1 near the bottom of one lateral adiabatic wall, relatively far from the opposite adiabatic lateral wall. Figure 12(a) shows an overshoot of the time evolution of D_{xy}^{**2} at $t^* \approx 5$. This time corresponds to that required by the fastest transported particles (namely those transported by the large-scale recirculation) to reach the top wall of the cavity and bend toward the horizontal direction (see Fig. 11, Multimedia available online). This change in direction produces a temporary reduction of the mean particle distance observed in the time evolution of D_{xy}^{**2}, and to a lesser extend in the time-evolution of D_{xyz}^{**2}. In contrast, the time-evolutions of Cloud#2 [Fig. 12(b)] show monotonic increases in the mean squared distances. Figure 12(a) shows that the largest variability associated with the mean separations is observed for the time-evolutions of D_z^{**2} indicating that within the large-scale circulation the fluctuations along the z direction is more intermittent compared with those in the x

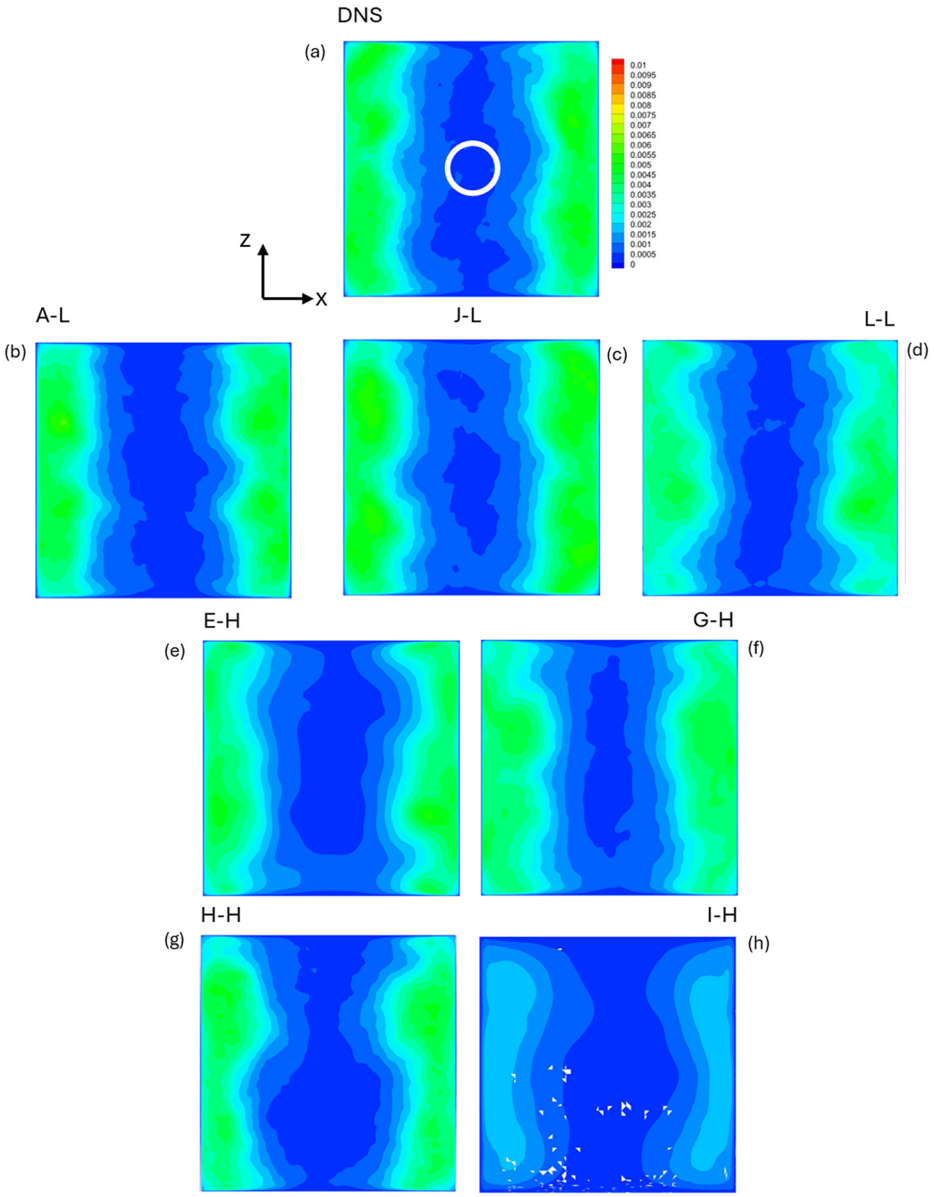

FIG. 8. Contours of the turbulence kinetic energy on the horizontal mid plane of the cavity ($y = 0$).

or y directions. The variabilities of the distances D^{**2}_{xyz} and D^{**2}_{xy} for Cloud#1 are similar and comparable with those for Cloud#2.

The comparisons between the time-evolutions of the mean separations of the different simulations with the mean values predicted by the DNS are plotted in Figs. 13–17. We grouped the plots according to the simulation technique used: Fig. 13 corresponds to LES, Fig. 14 to hybrid methods, Fig. 15 to SAS, Fig. 16 to URANS, and Fig. 17 to RANS.

Figure 13 shows that LES correctly predicts the dispersion of both clouds and that the times at which the mean distances reach the limiting values are comparable with those of DNS (i.e., $D^{**2}_{xyz} = D^{**2}_{xy} = D^{**2}_{z} = 1$ for $t^* \to \infty$). In contrast, the time evolution provided by the hybrid simulations, E-H, H-H and I-H, plotted in Fig. 14, reaches larger (E-H and H-H) or lower (I-H) limiting values in comparison with the theoretical ones, which are equal to unity. This can be attributed to non-uniform final distribution of the particles within the cavity attained at large times for these three simulations. For example, if particles tend to accumulate near the adiabatic walls, then the value of D^{*2}_{z} at large times will be larger than the theoretical one, $(D^{*2}_{z}(t \to \infty) = \frac{1}{6})$ and, thus, $D^{**2}_{z}(t \to \infty)$ will be higher than one (see, for example, Fig. 14(b).E-H). Conversely, if particles tend to accumulate near the center of the cavity, then $D^{*2}_{z}(t \to \infty) < 1$ (Fig. 14(b).I-H). On the other hand, the simulation G-H predicts correctly the time-evolutions of the different mean separations for the two

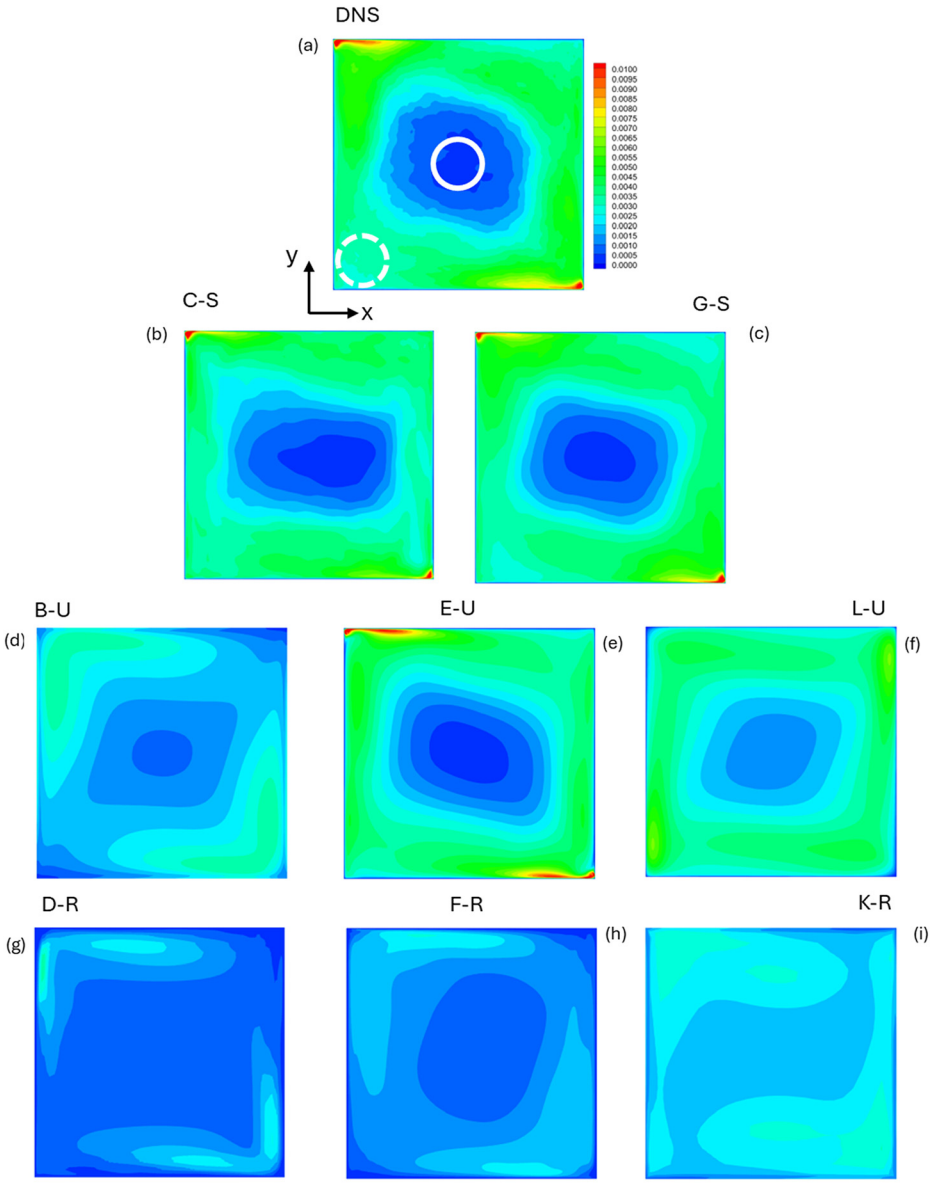

FIG. 9. Contours of the turbulence kinetic energy on the vertical symmetry plane of the cavity ($z = 0$).

clouds, as shown in Figs. 14(a).G-H and 14(b).G-H. From the information reported in Table III, it is difficult to infer the reason behind the better prediction of this hybrid simulation in comparison with simulations E-H, H-H, and I-H. However, inspecting the deviations, with respect to DNS, of the time-averaged velocity, temperature, and turbulence kinetic profiles shown in Fig. 6, reveals that, except for simulation I-H, the hybrid simulations (E-H, G-H, H-H) show similar deviations of the turbulence kinetic energy [Fig. 6(b)] but the velocity and temperature profiles of simulation G-H agree better with the DNS than those corresponding to simulations E-H, H-H, and I-H.

The time evolutions of the particle distances predicted by the two SAS are plotted in Fig. 15. Both simulations are within the variability of the dispersion of Cloud#1 provided by the different DNS realizations. For Cloud#2 [Figs. 15(b).C-S and 15(b).G-S] the dispersion is slightly underpredicted in the case of the simulation C-S while the simulation G-S agrees very well with the DNS. This agreement is also observed for the turbulence kinetic energy distributions shown in Figs. 9(b), 9(c), 10(b), and 10(c).

Figure 16 shows that the URANS simulation E-U reproduces the DNS fairly well, reaching a limiting value of the particle distances that is slightly larger than one. In contrast, simulations B-U and L-U and the three RANS simulations, plotted in Fig. 17, show significant deviations with respect to the DNS. In particular, these simulations underpredict the rate of dispersion of the particle clouds and this agrees with the low

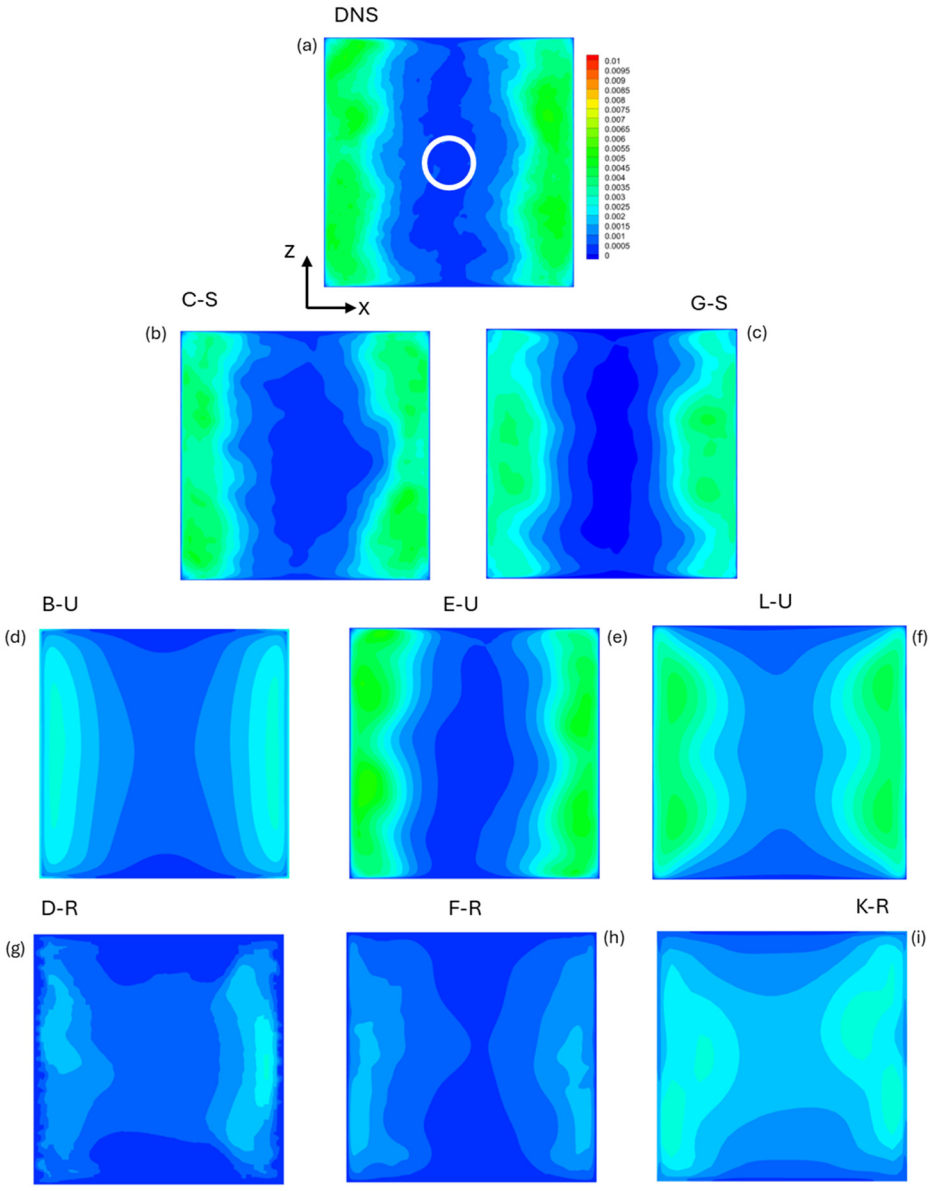

FIG. 10. Contours of the turbulence kinetic energy on the horizontal mid plane of the cavity ($y = 0$).

levels of turbulence kinetic energy obtained by the URANS and RANS simulations as shown in Figs. 9 and 10. These figures show that the simulation E-U predicts correctly the turbulence kinetic energy distribution while the other RANS (simulations D-R, F-R, and K-R) and URANS (B-U and L-U) systematically underestimate the overall turbulence level of the flow [see, for example, Figs. 9(d), 9(f), 9(g), 9(h), and 9(i)].

Lagrangian particle dispersion in hybrid methods and URANS/RANS flow simulations usually is performed employing stochastic models to incorporate the effect of the instantaneous turbulent fluctuations of the flow in the equations of particle motion (Mofakham and Ahmadi, 2020; Lo *et al.*, 2022). These models, often referred to as random walk models (RWMs), extract the fluctuating velocity from the mean flow solution to include the effect of the turbulent flow in the particle path. Commonly, simulations of turbulent flows using URANS and RANS techniques adopt the square root of the turbulence kinetic energy as the velocity scale to compute the fluctuating component of the particle velocity, which has been advected according to the time-averaged velocity field. For the flow conditions considered here, the turbulence kinetic energy peaks near the wall attaining non-dimensional values roughly equal to 4×10^{-3} (see Fig. 5). This yields a non-dimensional velocity scale for the fluctuations of approximately 0.06. This relatively large value, together with the insensitivity of most of the RWM implemented in commercial and open-source CFD codes to the direction of the fluctuations, can lead to an overestimation of

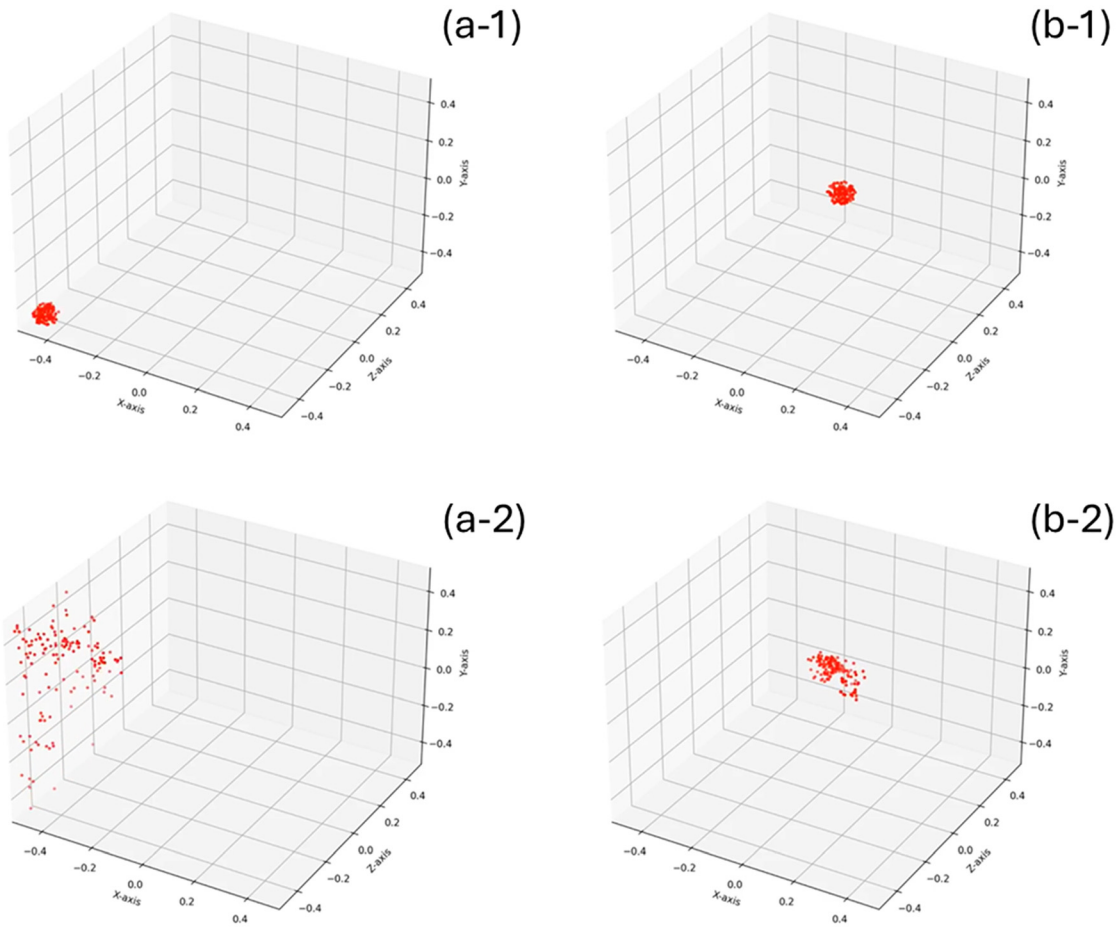

FIG. 11. Time evolution of the dispersion of the particles. (a) Cloud#1. (b) Cloud#2. (a-1) and (b-1) correspond to $t^* = 0$ and (a-2) and (b-2) to $t^* = 5$. Multimedia available online.

the particle velocity fluctuations toward the wall, artificially increasing particle-wall collisions and the injection of the particles very near the wall, where the particles get trapped due to the low mean velocity and turbulence kinetic energy. This scenario can lead to increased particle concentrations near the walls and produce deviations from the perfectly uniform distribution of particles within the cavity predicted by the DNS at large times ($t^* > 100$) and expected in view of the small Stokes number of the particles ($St = \frac{\rho_p d_p^2 V}{18\mu L} \sim 10^{-8}$).

To quantify the differences between the averaged values provided by the DNS and the predictions of D_{xyz}^{**2}, D_{xy}^{**2}, and D_z^{**2} of the different simulations, we use the deviation parameter, Φ, which was computed as follows. For each time evolution of D_{xyz}^{**2}, D_{xy}^{**2}, or D_z^{**2}, we identified the values that lay above the mean value plus one standard deviation of the DNS (reference DNS value, hereinafter). For these values we computed the absolute value of the difference with respect to the reference DNS value. The same procedure was then adopted for the values below the mean value minus one standard deviation of the DNS. Finally, the deviation parameter for the *i-th* mean squared separation (i.e., $i \equiv xyz$, xy or z) of the simulation *j-th* is defined as the averaged value of such differences

$$\Phi = \left\langle \mathrm{abs}\left[\left(D_i^{**2}(t)\right)^j - \left(D_i^{**2}(t)\right)^{DNS} \right] \right\rangle \tag{12}$$

if

$$\left(D_i^{**2}(t)\right)^j > \left(D_i^{**2}(t)\right)^{DNS} + \sigma\left(D_i^{**2}(t)\right)^{DNS}$$
$$or\ \left(D_i^{**2}(t)\right)^j < \left(D_i^{**2}(t)\right)^{DNS} - \sigma\left(D_i^{**2}(t)\right)^{DNS},$$

where $\sigma\left(D_i^{**2}(t)\right)^{DNS}$ is the standard deviation of the *i-th* mean squared separation predicted by the DNS. Figure 18 shows the deviation parameter for the three different mean particle distances of the two clouds and for the different simulations. The LES and hybrid simulations, in general, perform better than the RANS simulations. The exception is the simulation I-H, which shows significant differences, with respect to the DNS of the turbulence kinetic energy [see, for example, Fig. 8(h)]. Remarkably, the predictions of the SAS, C-S and

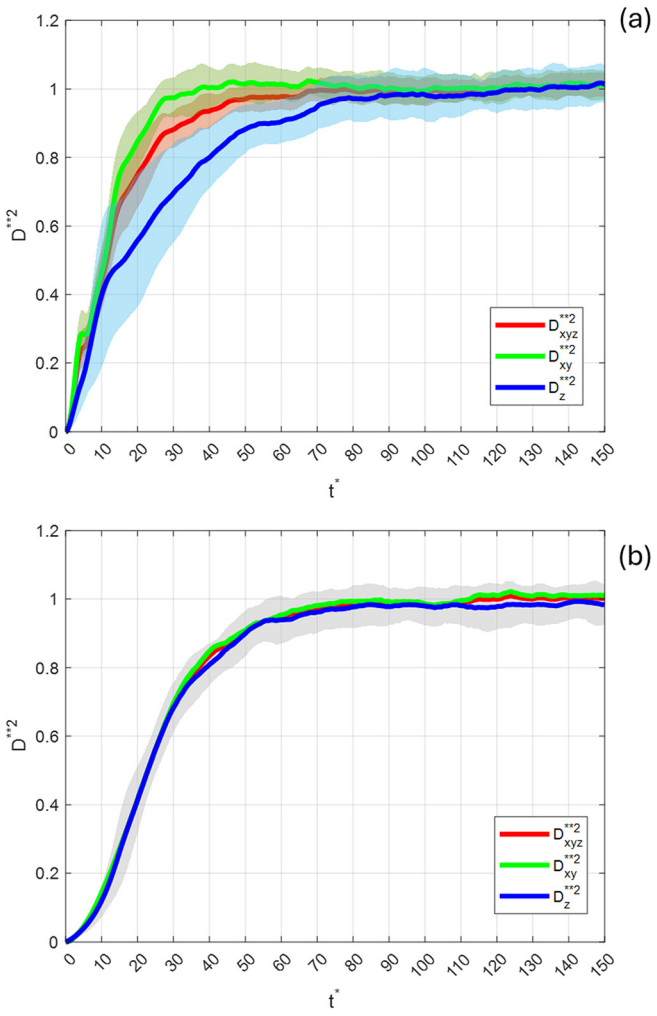

FIG. 12. Ensemble average time-evolutions of the non-dimensional mean squared particle separations. (a) Cloud#1. (b) Cloud#2.

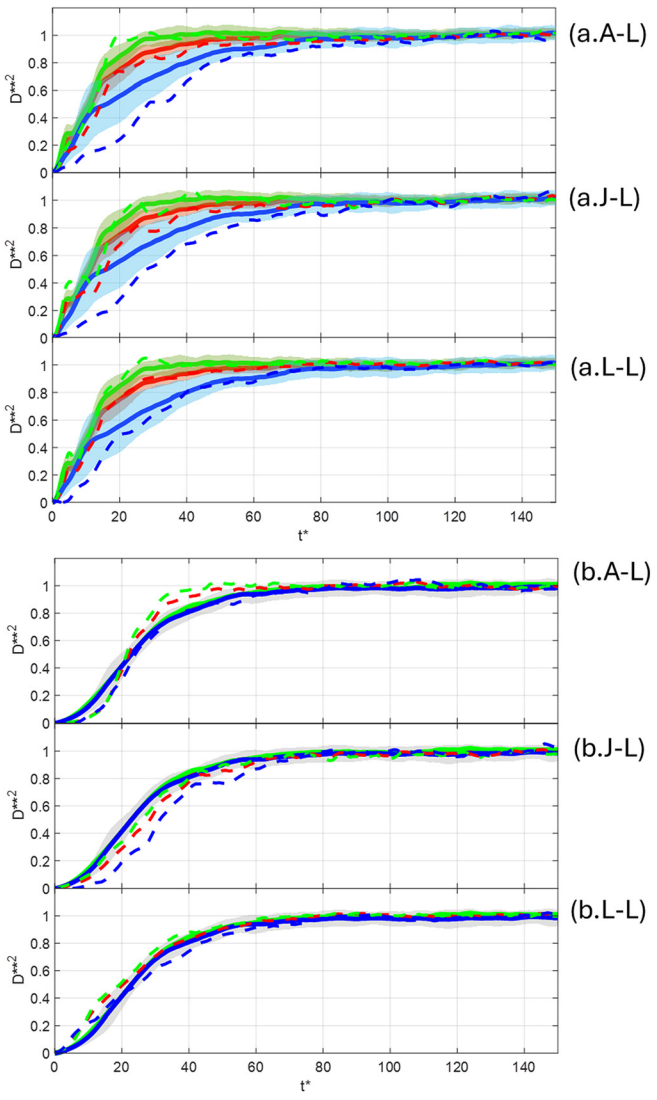

FIG. 13. Comparison LES/DNS of the time-evolutions of the non-dimensional mean squared particle separations. Red: D^{**2}_{xyz}. Green: D^{**2}_{xy}. Blue: D^{**2}_{z}. (a) Cloud#1. (b) Cloud#2.

G-S are also very close to the DNS, and they perform even better, in some cases, than some LES and hybrid simulations. The agreement with the DNS of the dispersion predicted by the URANS simulations depends strongly on the prediction of the turbulence kinetic energy distribution. For example, the simulation E-U with a similar distribution of the turbulence kinetic energy as the DNS [see Fig. 10(e)] is characterized by a lower deviation parameter than the simulations B-U and L-U. We recall here that the grid resolutions of these three URANS simulations are 0.4 M nodes for B-U and 2 M nodes for E-U and L-U and also that the turbulence models used are k-ε for B-U and L-U and k-ω for E-U (see Table III). This suggests that the better performance of the simulation E-U can be attributed to the combination of an adequate grid resolution together with the use of the k-ω turbulence model.

To summarize the comparison of the different simulations, we plotted in Fig. 19 the differences, with respect to DNS, of the information shown in two previous figures: Fig. 6, corresponding to the deviations of the profiles of velocity, temperature, and turbulence kinetic energy and Fig. 18, corresponding to the deviations of the particle dispersion. For each simulation, we have averaged the four bars of Fig. 6(a), the two bars of Fig. 6(b) and the six bars of Fig. 18, scaling the resulting averaged values with the mean for all the simulations. These scaled deviations are plotted in Fig. 19 and are accompanied by three bars. The blue bar indicates jointly the differences in the velocity and temperature profiles, the red bar corresponds to the differences in the turbulence kinetic energy and the orange bar to the difference in the particle dispersion. It can be seen that, in general, significant deviations of the turbulence kinetic energy leads to relatively large deviations of the particle dispersion. The exception is the simulation L-U

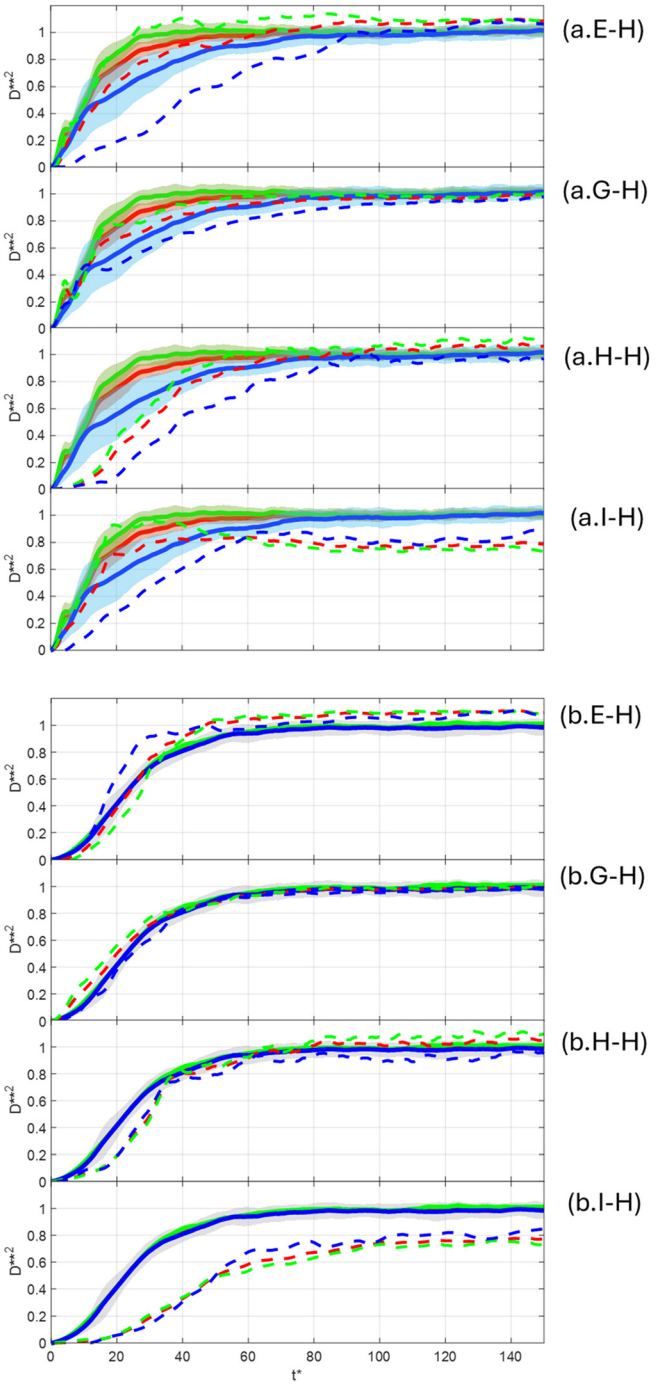

FIG. 14. Comparison hybrid simulations/DNS of the time-evolutions of the non-dimensional mean squared particle separations. Red: D^{**2}_{xyz}. Green: D^{**2}_{xy}. Blue: D^{**2}_{z}. (a) Cloud#1. (b) Cloud#2.

which shows good agreement with the DNS when comparing the turbulence kinetic energy profiles [Figs. 5(b) and 5(d)] but shows substantial differences when considering the spatial distributions of the turbulence kinetic energy [compare, for example, Figs. 10(a) and

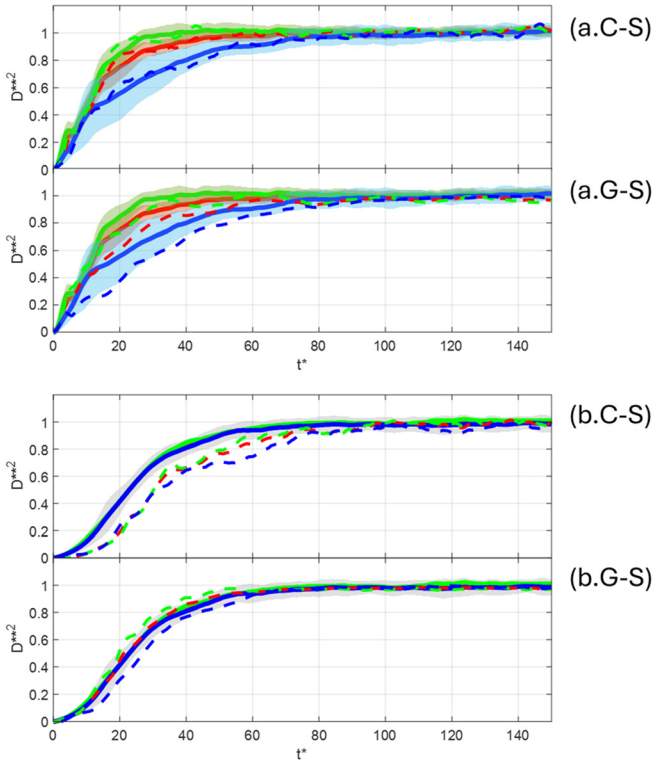

FIG. 15. Comparison SAS/DNS of the time-evolutions of the non-dimensional mean squared particle separations. Red: D^{**2}_{xyz}. Green: D^{**2}_{xy}. Blue: D^{**2}_{z}. (a) Cloud#1. (b) Cloud#2.

10(f)]. The differences in the velocity and temperature profiles are not strongly correlated with the differences in the particle dispersion. For example, simulations A-L and E-U show differences in the velocity and temperature profiles but predict reasonably well the cloud dispersion.

IV. CONCLUSIONS

In this paper, we presented and discussed the outcomes of a benchmark study conducted within the framework of an International CFD challenge. The study aimed to assess the performance of various numerical and turbulence modeling techniques to simulate the turbulent free convection flow and the dispersion of particles within a room-sized enclosure. Twelve research teams have contributed to the challenge and individually conducted a total of fifteen simulations of the same flow configuration, for which a reference direct numerical simulation (DNS) is available. The database generated consists of three large-eddy simulations (LES), four hybrid LES/RANS (Reynolds-Averaged Navier-Stokes) simulations, two Scale Adaptive Simulations (SAS), three unsteady Reynolds-averaged Navier–Stokes (URANS) simulations, and three RANS simulations. Results of the mean flow quantities and metrics of the dispersion of two clouds of particles are compared with each other and with the DNS results.

The mean flow quantities, the surface averaged Nusselt numbers, time-averaged velocity and temperature profiles, and the turbulence kinetic energy are, in general, well reproduced by the LES and the

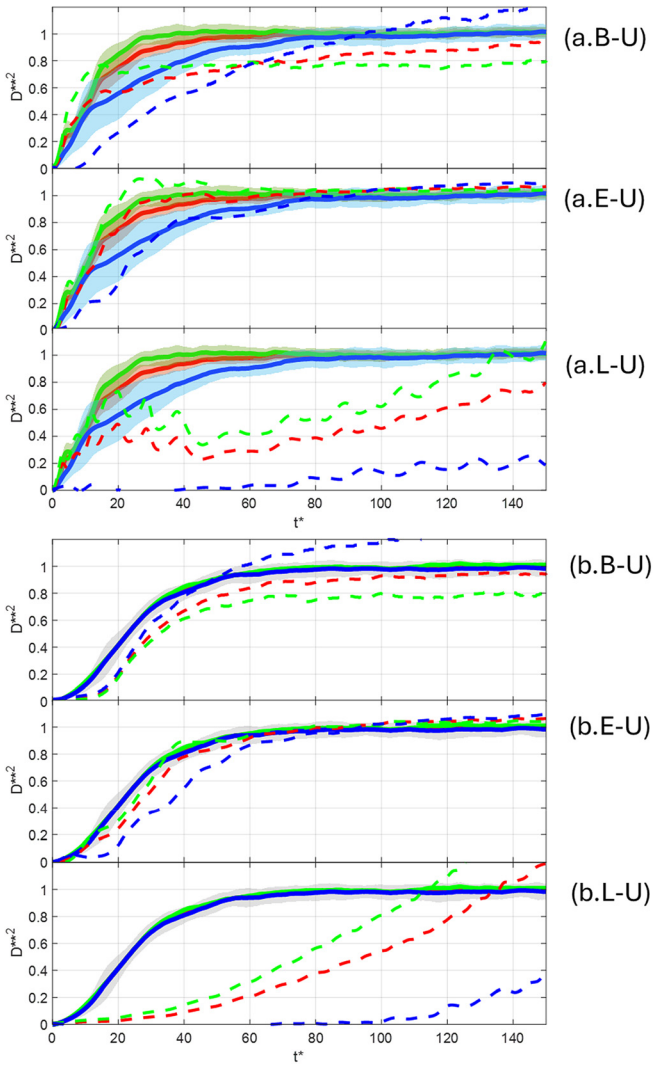

FIG. 16. Comparison URANS/DNS of the time-evolutions of the non-dimensional mean squared particle separations. Red: D^{**2}_{xyz}. Green: D^{**2}_{xy}. Blue: D^{**2}_{z}. (a) Cloud#1. (b) Cloud#2.

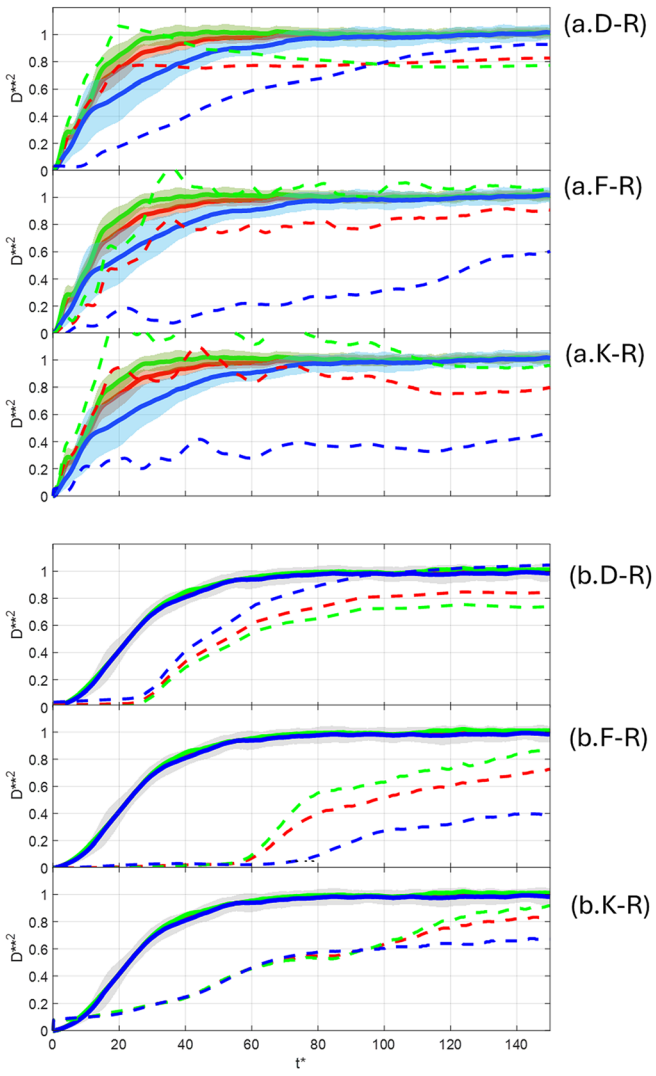

FIG. 17. Comparison RANS/DNS of the time-evolutions of the non-dimensional mean squared particle separations. Red: D^{**2}_{xyz}. Green: D^{**2}_{xy}. Blue: D^{**2}_{z}. (a) Cloud#1. (b) Cloud#2.

hybrid methods. In the case of different simulations performed with hybrid methods the grid resolution seems to be the cause for significant deviations when the grid is too coarse: In particular, this is observed for simulations performed with less than 2M nodes while simulations carried out with 2M nodes or more show much better agreement with the DNS. The two SAS simulations performed with similar grid resolutions as the hybrid simulations both show relatively small deviations, comparable with those provided by the LES or the hybrid simulations. The comparison of the three URANS cases shows that the one performed with the k-ω turbulence model has a better agreement with DNS than the one carried out with the same grid resolution (2M nodes) but using the k-ε model. The third URANS simulation, carried out with less than a quarter of the number of grid nodes used by the other two and using the k-ε model, shows larger deviations from DNS, as expected. The RANS simulations also exhibit significant differences with respect to DNS, independent of the grid resolution and the specific turbulence model (k-ε or k-ω) used.

The accuracy of particle dispersion predictions is primarily influenced by the combination of the turbulence model and grid resolution, as the choice of these factors plays a crucial role in accurately reproducing the turbulence kinetic energy. In fact, LES, hybrid simulations and URANS that properly predict the spatial distribution of the turbulence kinetic energy are found to capture the time evolutions of the mean squared separation of the particles, and, thus, the particle dispersion, in good agreement with DNS. Conversely, RANS simulations and coarse-grid hybrid simulations that underpredict the overall turbulence intensity of the flow, underpredict the rate of dispersion of the

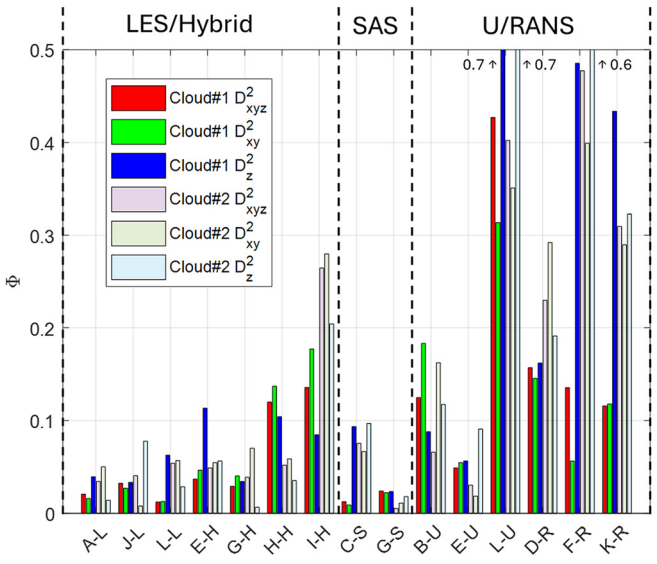

FIG. 18. Differences of the time evolutions of the mean squared particle separations predicted by the different simulations and the DNS.

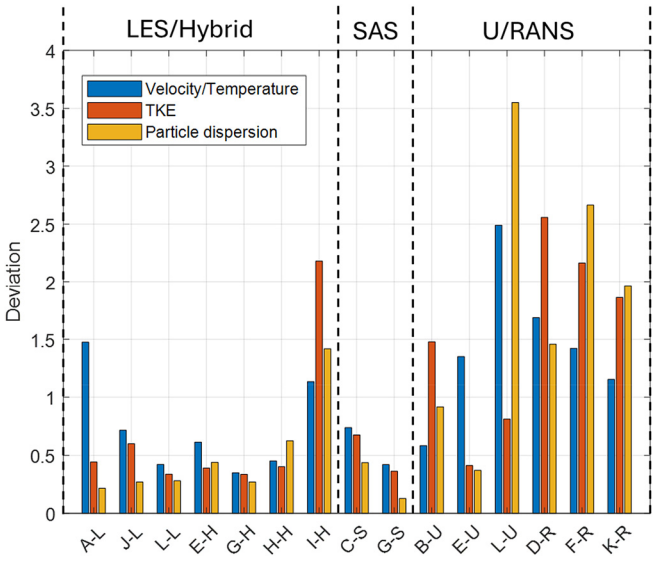

FIG. 19. Deviations, with respect to the DNS, of the time-averaged velocity/temperature fields, the turbulent kinetic energy and the particle dispersion.

particle clouds, and fail in capturing, for the flow conditions considered, the ultimate perfectly uniform distribution of the particles within the cavity.

SUPPLEMENTARY MATERIAL

See the supplementary material for the details of the turbulence models employed in the simulations, as well as information about the models used for the various terms in the particle force balance.

ACKNOWLEDGMENTS

B.F. and A.M. acknowledge the use of ARCHER2 UK National Supercomputing Service. (https://www.archer2.ac.uk).

D.F.F. and K.I. acknowledge the use of the National Computational Infrastructure (NCI) which is supported by the Australian Government and accessed through the Sydney Informatics Hub HPC Allocation Scheme, which is supported by the Deputy Vice-Chancellor (Research), University of Sydney.

F.D. and S.S. acknowledge the access to the HPC resources of Curie/Irene Rome from TGCC under the allocation A0162A06074 made by GENCI.

J.N. acknowledges funding by the MWK Baden-Württemberg (ref. no. 32-7545.20/4/59 Mittelbauprogramm).

J.P., A.F., A.L., and S.C. acknowledge the financial funding of projects PID2020-113303GB-C21 and PID2023-146648NB-C21, funded by the Spanish Ministerio de Ciencia e Innovación and the Agencia Estatal de Investigación and the support of the Departament de Recerca i Universitats de la Generalitat de Catalunya under project. 2021SGR00732.

J. S. and D. F. would like to acknowledge the financial support from the National Counsel of Technological and Scientific Development (CNPq) and Coordination for the Improvement of Higher Education Personnel - Brazil (CAPES) - Finance Code 001.

AUTHOR DECLARATIONS

Conflict of Interest

The authors have no conflicts to disclose.

Author Contributions

Jordi Pallares: Conceptualization (equal); Funding acquisition (equal); Investigation (equal); Resources (equal); Supervision (equal); Validation (equal); Writing – original draft (equal); Writing – review & editing (equal). **Bruño Fraga:** Data curation (equal); Investigation (equal); Validation (equal); Writing – review & editing (equal). **Aleksandra Monka:** Data curation (equal); Investigation (equal); Validation (equal); Writing – review & editing (equal). **Manuel Martínez:** Data curation (equal); Investigation (equal); Validation (equal); Writing – review & editing (equal). **Naomi Mestre-Curto:** Data curation (equal); Investigation (equal); Validation (equal); Writing – review & editing (equal). **Francisco Jose de Souza:** Data curation (equal); Investigation (equal); Validation (equal); Writing – review & editing (equal). **Douglas Fontes:** Data curation (equal); Investigation (equal); Validation (equal); Writing – review & editing (equal). **Natalie Jüngling:** Data curation (equal); Investigation (equal); Validation (equal); Writing – review & editing (equal). **Jennifer Niessner:** Data curation (equal); Investigation (equal); Validation (equal); Writing – review & editing (equal). **Robert Castilla:** Data curation (equal); Investigation (equal); Validation (equal); Writing – review & editing (equal). **Mercè Garcia Vílchez:** Data curation (equal); Investigation (equal); Validation (equal); Writing – review & editing (equal). **Alexandre Fabregat:** Conceptualization (equal); Data curation (equal); Investigation (equal); Supervision (equal); Validation (equal); Writing – original draft (equal); Writing – review & editing (equal). **David F. Fletcher:** Data curation (equal); Investigation (equal); Validation (equal); Writing – review & editing (equal). **Kiao Inthavong:** Data curation (equal); Investigation (equal); Validation (equal); Writing – review & editing (equal). **Matjaz Hribersek:** Data

curation (equal); Investigation (equal); Validation (equal); Writing – review & editing (equal). **Paul Steinmann:** Data curation (equal); Investigation (equal); Validation (equal); Writing – review & editing (equal). **Jana Wedel:** Data curation (equal); Investigation (equal); Validation (equal); Writing – review & editing (equal). **Florent Duchaine:** Data curation (equal); Investigation (equal); Validation (equal); Writing – review & editing (equal). **Shriram Sankurantripati:** Data curation (equal); Investigation (equal); Validation (equal); Writing – review & editing (equal). **Leo Amari:** Data curation (equal); Investigation (equal); Validation (equal); Writing – review & editing (equal). **Gábor Janiga:** Data curation (equal); Investigation (equal); Validation (equal); Writing – review & editing (equal). **Cristian Marchioli:** Conceptualization (equal); Methodology (equal); Resources (equal); Supervision (equal); Validation (equal); Writing – original draft (equal); Writing – review & editing (equal). **Akim Lavrinenko:** Conceptualization (equal); Data curation (equal); Investigation (equal); Validation (equal); Writing – review & editing (equal). **Salvatore Cito:** Conceptualization (equal); Methodology (equal); Resources (equal); Supervision (equal); Validation (equal); Writing – original draft (equal); Writing – review & editing (equal). **Nelson Marques:** Data curation (equal); Investigation (equal); Validation (equal); Writing – review & editing (equal). **Bruno Santos:** Data curation (equal); Investigation (equal); Validation (equal); Writing – review & editing (equal). **Gabriele Mosca:** Data curation (equal); Investigation (equal); Validation (equal); Writing – review & editing (equal). **Pedro Obando Vega:** Data curation (equal); Investigation (equal); Validation (equal); Writing – original draft (equal). **Jure Ravnik:** Data curation (equal); Investigation (equal); Validation (equal); Writing – review & editing (equal). **Nejc Vovk:** Data curation (equal); Investigation (equal); Validation (equal); Writing – review & editing (equal).

DATA AVAILABILITY

The data that support the findings of this study are available from the corresponding author upon reasonable request.

REFERENCES

Ai, Z. T. and Melikov, A. K., "Airborne spread of expiratory droplet nuclei between the occupants of indoor environments: A review," Indoor air **28**(4), 500–524 (2018).

See https://www.ansys.com/products/fluids/ansys-fluent for "Ansys Fluent" (2024).

Bournet, P. E. and Boulard, T., "Effect of ventilator configuration on the distributed climate of greenhouses: A review of experimental and CFD studies," Comput. Electron. Agric. **74**(2), 195–217 (2010).

Bourouiba, L., "Fluid dynamics of respiratory infectious diseases," Annu. Rev. Biomed. Eng. **23**(1), 547–577 (2021).

Caciolo, M., Stabat, P., and Marchio, D., "Numerical simulation of single-sided ventilation using RANS and LES and comparison with full-scale experiments," Build. Environ. **50**, 202–213 (2012).

Choi, H., Kim, H., and Kim, T., "Long-term simulation for predicting indoor air pollutant concentration considering pollutant distribution based on concept of CRPS index," in *Building Simulation* (Tsinghua University Press, 2019), Vol. 12, pp. 1131–1140.

Concilio, C., Benito, P. A., Ramírez, C. P., and Viccione, G., "CFD simulation study and experimental analysis of indoor air stratification in an unventilated classroom: A case study in Spain," Heliyon **10**, e32721 (2024).

Cuce, E., Sher, F., Sadiq, H., Cuce, P. M., Guclu, T., and Besir, A. B., "Sustainable ventilation strategies in buildings: CFD research," Sustainable Energy Technol. Assess. **36**, 100540 (2019).

Dehbi, A., Kalilainen, J., Lind, T., and Auvinen, A., "A large eddy simulation of turbulent particle-laden flow inside a cubical differentially heated cavity," J. Aerosol Sci. **103**, 67–82 (2017).

Delort-Laval, M., Soucasse, L., Rivière, P., and Soufiani, A., "Rayleigh–Bénard convection in a cubic cell under the effects of gas radiation up to $Ra = 10^9$," Int. J. Heat Mass Transfer **187**, 122453 (2022).

Demou, A. D. and Grigoriadis, D. G., "Direct numerical simulations of Rayleigh–Bénard convection in water with non-Oberbeck–Boussinesq effects," J. Fluid Mech. **881**, 1073–1096 (2019).

Duchaine, F., Cizeron, C. N., Odier, N., Dombard, J., Marchall, S., Francois, N., and Poinsot, T., "High-performance CFD for respiratory droplet turbulent dispersion in a ventilated city bus," Int. J. Comput. Fluid Dyn. **35**(9), 758–777 (2021).

Fabregat, A. and Pallares, J., "Heat transfer and boundary layer analyses of laminar and turbulent natural convection in a cubical cavity with differently heated opposed walls," Int. J. Heat Mass Transfer **151**, 119409 (2020).

Fraga, B., Stoesser, T., Lai, C. C., and Socolofsky, S. A., "A LES-based Eulerian–Lagrangian approach to predict the dynamics of bubble plumes," Ocean Modell. **97**, 27–36 (2016).

Gilani, S., Montazeri, H., and Blocken, B., "CFD simulation of stratified indoor environment in displacement ventilation: Validation and sensitivity analysis," Build. Environ. **95**, 299–313 (2016).

Hanjalić, K. and Vasić, S., "Computation of turbulent natural convection in rectangular enclosures with an algebraic flux model," Int. J. Heat Mass Transfer **36**(14), 3603–3624 (1993).

Jones, A. P., "Indoor air quality and health," Atmos. Environ. **33**(28), 4535–4564 (1999).

Kalilainen, J., Rantanen, P., Lind, T., Auvinen, A., and Dehbi, A., "Experimental investigation of a turbulent particle-laden flow inside a cubical differentially heated cavity," J. Aerosol Sci. **100**, 73–87 (2016).

Lavrinenko, A., Fabregat, A., Gisbert, F., and Pallares, J., "Direct numerical simulation of pathogen-laden aerosol dispersion in buoyancy-driven turbulent flow within confined spaces," Int. Commun. Heat Mass Transfer **152**, 107272 (2024).

Lavrinenko, A., Gisbert, F., Pallares, J., and Fabregat, A., "Fully-resolved numerical simulations of the turbulent flow and particle deposition in a cubical cavity with two pairs of differentially heated opposed walls at Rayleigh number 3.6×10^9," Int. Commun. Heat Mass Transfer **141**, 106564 (2023).

Li, Y. and Nielsen, P. V., "CFD and ventilation research," Indoor Air **21**(6), 442–453 (2011).

Li, Z., Wen, Q., and Zhang, R., "Sources, health effects and control strategies of indoor fine particulate matter (PM2. 5): A review," Sci. Total Environ. **586**, 610–622 (2017).

Lo, C., Bons, J., Yao, Y., and Capecelatro, J., "Assessment of stochastic models for predicting particle transport and deposition in turbulent pipe flows," J. Aerosol Sci. **162**, 105954 (2022).

Maity, P., Koltai, P., and Schumacher, J., "Large-scale flow in a cubic Rayleigh–Bénard cell: Long-term turbulence statistics and Markovianity of macrostate transitions," Philos. Trans. R. Soc. London, Ser. A **380**(2225), 20210042 (2022).

Maroni, M., Seifert, B., and Lindvall, T., *Indoor Air Quality: A Comprehensive Reference Book* (Elsevier, 1995).

Mofakham, A. A. and Ahmadi, G., "On random walk models for simulation of particle-laden turbulent flows," Int. J. Multiphase Flow **122**, 103157 (2020).

Monka, A., Fraga, B., Soper, D., and Hemida, H., "Influence of thermal stratification on the transport of polydispersed expiratory particles," Phys. Fluids **35**(10), 103304 (2023).

See https://www.paraview.org/ for "Paraview" (2024).

Riley, W. J., McKone, T. E., Lai, A. C., and Nazaroff, W. W., "Indoor particulate matter of outdoor origin: Importance of size-dependent removal mechanisms," Environ. Sci. Technol. **36**(2), 200–207 (2002).

Salat, J., Xin, S., Joubert, P., Sergent, A., Penot, F., and Le Quere, P., "Experimental and numerical investigation of turbulent natural convection in a large air-filled cavity," Int. J. Heat Fluid Flow **25**(5), 824–832 (2004).

Scheel, J. D. and Schumacher, J., "Local boundary layer scales in turbulent Rayleigh–Bénard convection," J. Fluid Mech. **758**, 344–373 (2014).

Scheel, J. D., Emran, M. S., and Schumacher, J., "Resolving the fine-scale structure in turbulent Rayleigh–Bénard convection," New J. Phys. **15**(11), 113063 (2013).

Schønfeld, T. and Rudgyard, M., "Steady and unsteady flow simulations using the hybrid flow solver AVBP," AIAA J. **37**(11), 1378–1385 (1999).
Seguel, J. M., Merrill, R., Seguel, D., and Campagna, A. C., "Indoor air quality," Am. J. Lifestyle Med. **11**(4), 284–295 (2017).
Sheikhnejad, Y., Aghamolaei, R., Fallahpour, M., Motamedi, H., Moshfeghi, M., Mirzaei, P. A., and Bordbar, H., "Airborne and aerosol pathogen transmission modeling of respiratory events in buildings: An overview of computational fluid dynamics," Sustainable Cities Soc. **79**, 103704 (2022).
Shen, C., Gao, N., and Wang, T., "CFD study on the transmission of indoor pollutants under personalized ventilation," Build. Environ. **63**, 69–78 (2013).
Shim, G., Narayanan, S. R., and Yang, S., "Numerical simulation of virus-laden aerosol transmission in real human respiratory airways," Phys. Fluids **35**(10), 101903 (2023).
Soucasse, L., Podvin, B., Rivière, P., and Soufiani, A., "Proper orthogonal decomposition analysis and modelling of large-scale flow reorientations in a cubic Rayleigh–Bénard cell," J. Fluid Mech. **881**, 23–50 (2019).
See https://www.plm.automation.siemens.com/global/en/products/simcenter/STAR-CCM.html for "STAR-CCM+" (2024).
Tan, Z. and Zhang, Y., "An overview of particulate matter in indoor environments: Sources and effects," ASHRAE Trans. **109**, 89–100 (2003).
Teimurazov, A., Reiter, P., Shishkina, O., and Frick, P., "Heat transport in a cell heated at the bottom and the side," Europhys. Lett. **134**(3), 34001 (2021).
Tric, E., Labrosse, G., and Betrouni, M., "A first incursion into the 3D structure of natural convection of air in a differentially heated cubic cavity, from accurate numerical solutions," Int. J. Heat Mass Transfer **43**(21), 4043–4056 (2000).
van Hooff, T., Blocken, B., and Tominaga, Y., "On the accuracy of CFD simulations of cross-ventilation flows for a generic isolated building: Comparison of RANS, LES and experiments," Build. Environ. **114**, 148–165 (2017).
Vasiliev, A., Frick, P., Kumar, A., Stepanov, R., Sukhanovskii, A., and Verma, M. K., "Transient flows and reorientations of large-scale convection in a cubic cell," Int. Commun. Heat Mass Transfer **108**, 104319 (2019).
Velasco, L. J., Venturi, D. N., Fontes, D. H., and de Souza, F. J., "Numerical simulation of drag reduction by microbubbles in a vertical channel," Eur. J. Mech. B. Fluids **92**, 215–225 (2022).
Villafruela, J. M., Olmedo, I., De Adana, M. R., Méndez, C., and Nielsen, P. V., "CFD analysis of the human exhalation flow using different boundary conditions and ventilation strategies," Build. Environ. **62**, 191–200 (2013).
Wang, P., Zhang, Y., and Guo, Z., "Numerical study of three-dimensional natural convection in a cubical cavity at high Rayleigh numbers," Int. J. Heat Mass Transfer **113**, 217–228 (2017).
Weller, H., Tabor, G., Jasak, H., and Fureby, C., "A tensorial approach to computational continuum mechanics using object-oriented techniques," Comput. Phys. **12**, 620 (1998).
World Health Organization, Regional Office for Europe, *WHO Guidelines for Indoor Air Quality: Selected Pollutants* (World Health Organization, Regional Office for Europe, 2010).
Xu, G. and Wang, J., "CFD modeling of particle dispersion and deposition coupled with particle dynamical models in a ventilated room," Atmos. Environ. **166**, 300–314 (2017).
Yang, R., Ng, C. S., Chong, K. L., Verzicco, R., and Lohse, D., "Do increased flow rates in displacement ventilation always lead to better results?," J. Fluid Mech. **932**, A3 (2022).
Yerragolam, G. S., Howland, C. J., Yang, R., Stevens, R. J., Verzicco, R., and Lohse, D., "Effect of airflow rate on CO_2 concentration in downflow indoor ventilation," Indoor Environ. **1**(2), 100012 (2024).